Monthly Notices of the ROYAL ASTRONOMICAL SOCIETY

MNRAS **504,** 2924–2939 (2021) doi:10.1093/mnras/stab964
Advance Access publication 2021 April 9

A MeerKAT view on galaxy clusters: a radio–optical study of Abell 1300 and MACS J1931.8−2634

B. Terni de Gregory,[1,2]★ B. Hugo,[3,4] T. Venturi,[1] G. Bernardi,[1,3,4] D. Dallacasa,[1,2] M. Nonino,[5] S. Makhatini,[3] V. Parekh,[3] O. M. Smirnov,[3,4] S. Giacintucci[6] and R. Kale[7]

[1]*INAF – Istituto di Radio Astronomia, Via Gobetti 101, I-40129 Bologna, Italy*
[2]*Dipartimento di Fisica e Astronomia, Universitá di Bologna, Via Gobetti 93/2, I-40129 Bologna, Italy*
[3]*South African Radio Astronomy Observatory, Black River Park, 2 Fir Street, Observatory, Cape Town 7925, South Africa*
[4]*Department of Physics and Electronics, Rhodes University, PO Box 94, Grahamstown 6140, South Africa*
[5]*INAF – Osservatorio Astronomico di Trieste, Via G. B. Tiepolo 11, I-34143 Trieste, Italy*
[6]*Naval Research Laboratory, 4555 Overlook Avenue SW, Code 7213, Washington, DC 20375, USA*
[7]*National Centre for Radio Astrophysics, Tata Institute of Fundamental Research, S. P. Pune University Campus, Ganeshkhind, Pune 411007, Maharashtra, India*

Accepted 2021 March 30. Received 2021 March 26; in original form 2020 July 18

ABSTRACT

In this paper, we present results from a radio–optical study of the galaxy populations of the galaxy clusters Abell 1300 and MACS J1931.8−2634, a merger and a relaxed system respectively both located at $z \sim 0.3$, aimed at finding evidence of merger-induced radio emission. Radio observations are taken at 1.28 GHz with the MeerKAT interferometer during its early-stage commissioning phase, and combined with archive optical data. We generated catalogues containing 107 and 162 radio sources in the A 1300 and MACS J1931.8−2634 cluster fields, respectively, above a 0.2 mJy threshold and within a 30 arcmin radius from the cluster centre (corresponding to 8.1 and 8.8 Mpc, respectively). By cross-correlating the radio and optical catalogues, and including spectroscopic information, nine and six sources were found to be cluster members and used to construct the radio luminosity functions, respectively, for both clusters. The comparison of the radio source catalogues between the two cluster fields leads to a marginal difference, with a 2σ statistical significance. We derived the radio luminosity function at 1.28 GHz in both clusters, in the power range of $22.81 < \log P_{1.28\ \mathrm{GHz}}\ (\mathrm{W\,Hz^{-1}}) < 25.95$, and obtained that in A 1300 the radio luminosity function averaged over the full radio power interval is only 3.3 ± 1.9 times higher than the MACS J1931.8−2634 one, suggesting no statistical difference in their probability to host nuclear radio emission. We conclude that, at least for the two clusters studied here, the role of cluster mergers in affecting the statistical properties of the radio galaxy population is negligible.

Key words: galaxies: clusters: general – galaxies: clusters: individuals: A 1300, MACS J1931.8−2634 – galaxies: evolution – galaxies: general.

1 INTRODUCTION

Cluster mergers are the most energetic events in the Universe. They are the natural way of forming rich clusters of galaxies within cold dark matter scenarios, which imply a bottom-up hierarchy of structure formation (Press & Schechter 1974; Sarazin 2002). The merging process generates important perturbations in the intra-cluster medium such as shocks, bulk flows, and turbulence in the hot gas, which considerably affect the properties of the non-thermal components of galaxy clusters. As a matter of fact, it is nowadays well established that the spectacular cluster-scale radio emission in the form of haloes and relics originates from merging processes (see Brüggen et al. 2012; Brunetti & Jones 2014; Botteon et al. 2016, and references therein).

While the morphology of radio galaxies is strongly affected by the environment, as witnessed by the presence of wide-angle tails (WATs) and narrow-angle tails (NATs) in the majority of galaxy clusters and groups (see Feretti & Venturi 2002, for a review on the topic), the role of cluster formation processes on the statistical radio properties of the galaxy population is still unclear. The most powerful tool to investigate the influence of the environment on the radio properties of galaxies is the radio luminosity function (RLF), which gives the probability for a galaxy to develop a radio source above a given radio power threshold. The comparison of RLFs for galaxies in different environments and at different redshifts provides clues on the role of the environment and of the cosmological evolution. To date, results of these studies are, however, inconclusive. The few clusters studied in detail so far in the local Universe provide conflicting results both for the radio nuclear activity and for the starburst population of galaxies (Dwarakanath & Owen 1999; Owen et al. 1999; Venturi et al. 2000, 2001; Miller & Owen 2003; Giacintucci et al. 2004), suggesting that several parameters might play a relevant role.

The cosmological evolution of the RLF is a matter of debate, too. Studies of clusters at intermediate redshift ($0.3 < z < 0.8$) provide different results for different samples (Stocke et al. 1999; Branchesi

★ E-mail: giannibernardi75@gmail.com

© 2021 The Author(s)
Published by Oxford University Press on behalf of Royal Astronomical Society

Downloaded from https://academic.oup.com/mnras/article/504/2/2924/6219094 by CNR BOLOGNA AREA DELLA RICERCA user on 17 March 2022

et al. 2006; Gralla et al. 2011) when compared to the local RLF of cluster galaxies (Ledlow & Owen 1996).

The only solid results are the dependence of the RLF on the optical magnitude of the host galaxy, at least up to $z = 0.3$ (Mauch & Sadler 2007), and the remarkably different behaviour of the brightest cluster galaxies (BCGs) in relaxed and merging clusters in the GMRT Radio Halo cluster sample (Kale et al. 2015) and for the HIFLUG cluster sample at lower redshift (Mittal et al. 2009). These show that the fraction of BCGs with radio emission is much higher in relaxed clusters at least up to $z = 0.4$, and increases with increasing cool-core strength.

During the MeerKAT-16 commissioning stage, we observed the two galaxy clusters Abell 1300 (A 1300) and MACS J1931.8−2634. While the main goal of the observations was to test the telescope performance and new calibration and imaging procedures, the galaxy clusters were selected with the scientific aim to address the role of cluster mergers in shaping the radio properties of cluster radio galaxies. The two clusters are at similar redshifts ($z \sim 0.3$) and have similar mass, but they differ in their dynamical properties: A 1300 is considered a post-merger, while MACS J1931.8−2634 is classified as a relaxed system. The two clusters were observed at 1.28 GHz with the MeerKAT array, and the radio observations were complemented with optical *Subaru*-SuprimeCam images for a comparative study of the radio galaxy population in two different environments, which we carried out comparing their radio source counts and their RLFs.

In this paper, we present the results of our study. The layout is as follows: Section 2 describes the observations and data reduction; the optical data are described in Section 3; radio catalogues, source counts, optical IDs, and RLFs are shown in Section 4 and conclusions are presented in Section 5. Throughout the paper, we assume $H_0 = 70$ km s^{-1} Mpc^{-1}, $\Omega_m = 0.3$, and $\Omega_\Lambda = 0.7$, which give 4.5 and 4.9 kpc arcsec^{-1} scales for A 1300 and MACS J1931.8−2634, respectively.

1.1 A 1300

The galaxy cluster A 1300 is reported as a $z = 0.31$, richness class 1 object by Abell, Corwin Harold & Olowin (1989). It was first surveyed in the X-ray band during the *Rosat* All Sky Survey (Pierre et al. 1994), where it is identified with RXJ1131.9−1955. It has an X-ray luminosity (L_x) of $\sim 1.7 \times 10^{45}$ erg s^{-1} in the 0.1–2.4 keV band and a mass (M) of $\sim 1.3 \times 10^{15}$ M$_\odot$ (Lemonon et al. 1997). Its virial radius is 1.53 Mpc, corresponding to 5.7 arcmin (Ziparo et al. 2012).

Optical (Pierre et al. 1997) and X-ray (Lemonon et al. 1997) observations suggest that A 1300 is in a post-merging phase. It is estimated that a major merger occurred about 3 Gyr ago, with further accretion taking place along the cosmic web filaments, leading to an increase of the cluster mass up to 60 per cent in the next ∼Gyr (Ziparo et al. 2012). Ziparo et al. (2012) quote 987 km s^{-1} as rest-frame velocity dispersion, which they also use to estimate a dynamical mass (M_{200}) of $\approx 1.1 \times 10^{15}$ M$_\odot$. The cluster hosts a giant radio halo and a relic located in the south-western periphery of the cluster and a number of extended radio galaxies in the central regions (Reid et al. 1999; Venturi et al. 2013). A 1300 is among the targets of the Merging Cluster Collaboration (MCC),[1] and of the Galaxy Cluster at VirCam Survey (GCAV),[2] an infrared, 560 h, ESO Public Survey (PI: Nonino M.) in the *Y*, *J*, and *Ks* bands, whose aim is to explore galaxy evolution over a large variety of environments.

1.2 MACS J1931.8−2634

This massive ($M_{200} = 1.74 \times 10^{15}$ M$_\odot$; Umetsu et al. 2014), $z = 0.35$, cool-core galaxy cluster (Ebeling et al. 2010) is part of the Massive Cluster Survey sample (MACS; see Ebeling 2007, and references therein) and has an X-ray luminosity (L_x) of $\sim 2.2 \times 10^{45}$ erg s^{-1} in the 0.1–2.4 keV. It hosts one of the X-ray most luminous cool cores discovered so far, with an equivalent mass cooling rate within the central 50 h_{70}^{-1} kpc of ∼700 M$_\odot$ yr^{-1} (Ehlert et al. 2011). Its virial radius is 1.8 Mpc, corresponding to 6.1 arcmin (Santos et al. 2016).

Santos et al. (2016) report a weak-lensing mass (M_{200}) of $\approx 0.99 \times 10^{15}$ M$_\odot$ (see also Merten et al. 2015). For comparison with A 1300, from the mass we estimate a velocity dispersion following Carlberg, Yee & Ellingson (1997) (using the same cosmology as Ziparo et al. 2012), resulting in $\sigma \approx 900$ km s^{-1}, i.e. similar to A 1300. The two clusters are thus quite similar in mass, meaning, via the mass–richness scaling relation (Andreon & Hurn 2010; Melchior et al. 2017), that they have similar richness.

The BCG is surrounded by X-ray cavities created by an outburst from the central source (Allen et al. 2004) and is undergoing intense star formation (Donahue et al. 2015; Fogarty et al. 2015; Santos et al. 2016). Moreover, it is embedded in extended radio emission whose nature, i.e. radio lobes or minihalo, is still a matter of debate (Giacintucci et al. 2004, 2017). The cluster hosts a narrow-angle tailed (NAT) radio galaxy, located at ∼200 kpc linear projected distance south of the BCG. MACS J1931.8−2634 is part of the Cluster Lensing and Supernovae Survey with Hubble sample (CLASH; Postman et al. 2012).

2 MEERKAT OBSERVATIONS AND DATA REDUCTION

The MeerKAT radio telescope[3] is a precursor for the Square Kilometre Array mid-frequency telescope (Jonas & MeerKAT Team 2016; Camilo et al. 2018; Mauch et al. 2020). The full array consists of 64 antennas with 13.5-m-diameter dishes that operate with an effective bandwidth from 580 to 3500 MHz split into (at present) UHF, *L*-band, and *S*-band receivers. The array configuration consists of a 1 km inner core containing ≈70 per cent of the dishes and a distribution of antennas reaching a maximum baseline length of 8 km. The instrumental field of view spans roughly from 0.5° to 1° at the −20 dB point of the voltage beam, at the low and high ends of the *L*-band bandwidth (Jonas & MeerKAT Team 2016; Mauch et al. 2020). This wide field of view enables us to image far beyond the virial radii of the two clusters (i.e. ∼1.5 Mpc) for our statistical analysis.

The observations presented in this paper were performed during the Array Release 1.5 construction phase, i.e. when only 16 antennas were available. Details of the observations are reported in Table 1. The data were taken at the *L* band, with a central frequency of 1.283 GHz ($\lambda = 0.23$ m) and a total bandwidth of 852 MHz. The signal correlation was carried out using 4096 channels in total, each 208 kHz wide, with a 2 s integration time. Even though the observations of the two clusters were close in time, the array configuration differed, and this is reflected into the *uv* coverage, shown in Fig. 1 for both sources. The combination of the different *uv* coverage and more severe Radio Frequency Interference (RFI) excision led to a worse sampling of the *uv* plane and lower angular resolution for A 1300 (see also Table 1).

[1] http://www.mergingclustercollaboration.org/
[2] https://www.eso.org/sci/observing/PublicSurveys/docs/GCAV
[3] https://www.sarao.ac.za

Downloaded from https://academic.oup.com/mnras/article/504/2/2924/6219094 by CNR BOLOGNA AREA DELLA RICERCA user on 17 March 2022

Table 1. Details of the radio observations. From left to right: (1) observing date, (2) target name, (3) and (4) J2000 coordinates, (5) central observing frequency (ν_c), (6) bandwidth, (7) integration time, (8) full width at half-maximum and (9) position angle of the restoring beam, and (10) image noise.

(1) Obs. date	(2) Name	(3) RA_{J2000} (h m s)	(4) $Dec._{J2000}$ (° ' ")	(5) ν_c (MHz)	(6) BW (MHz)	(7) Int. time (h)	(8) FWHM (arcsec × arcsec)	(9) PA (deg)	(10) rms (mJy beam^{-1})
2018 April	A 1300	11:31:54.4	−19:55:42	1283	856	2.4	12 x 5	113	0.04
2018 May	MACS J1931.8−2634	19:31:49.6	−26:34:34	1283	856	2.0	5 x 3	136	0.04

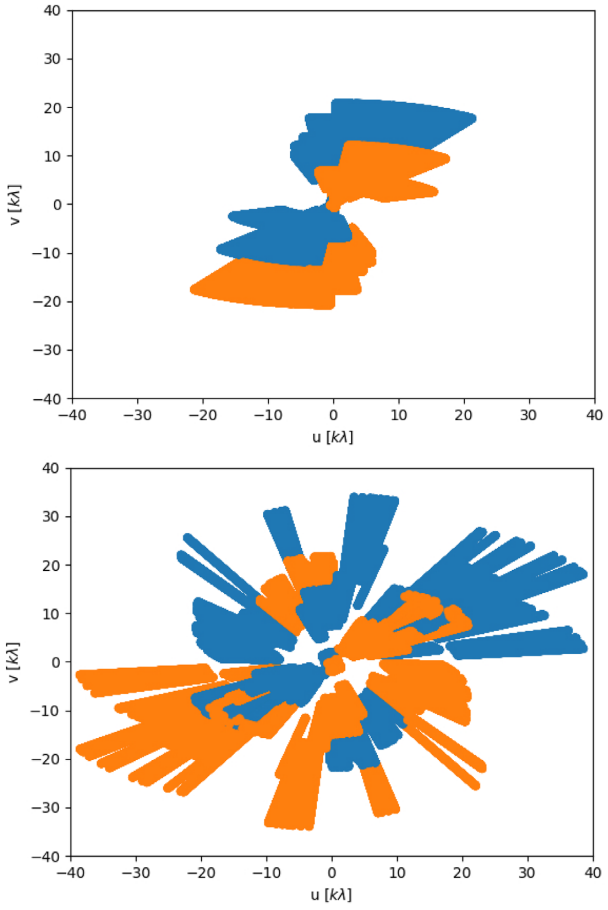

Figure 1. A 1300 (top panel) and MACS J1931.8−2634 (bottom panel) *uv* coverages over the entire bandwidth. Only 1 out of every 10 points in time and 1 out of every 40 points in frequency are plotted. The two colours show the symmetric *uv* points obtained from the conjugate visibilities. Note that the different *uv* coverage for the two clusters reflects into a different synthesized beam (Table 1).

The data reduction was carried out using the NRAO `Common Astronomy Software Application (CASA)` package (McMullin et al. 2007) for the a priori calibration and a combination of `CubiCal` (Kenyon et al. 2018) and `WSClean` (Offringa et al. 2014) for the self-calibration. Moreover, we used `DDFacet` (Tasse et al. 2018) to obtain the primary beam-corrected images. The packages were pipelined together by means of the containerized `Stimela` scripting platform (Makhathini 2018). To ensure self-consistency between the two fields, we adopted the same strategy for the bandpass calibration, imaging and self-calibration. The complex bandpass was derived from the observation of PKS B1934−638 (Reynolds 1994). RFI mitigation was accomplished using a combination of a static mask of known *L*-band interferences including band rolloffs, and residual autoflagging using `AOFLAGGER` (Offringa, van de Gronde & Roerdink 2012; Offringa et al. 2013). Multiple rounds of flagging and calibration were performed to remove residual narrow-band RFI.

The complex bandpass was applied to the target, and the data were averaged by a factor of 2 in frequency (obtaining a 416 kHz channel width). The number of channels on which we performed the direction-independent self-calibration became 2048. The final effective bandwidth after RFI removal (which excludes the band edges) is about 750 MHz.

Self-calibration was then performed with a combination of non-parametric time-variable gains using CubiCal and sky models synthesized using the wide-field, wide-band WSClean imager. The initial model images were deconvolved down to a 0.2 mJy threshold (5σ). The self-calibration was performed by four iterations with phase-only solutions. The solution interval was reduced inspecting the solutions at each step. Each imaging step in the self-calibration cycle was carried out with Briggs weighting scheme −2 (Briggs 1995) to achieve the maximum resolution needed to fulfil our scientific goals. Deconvolution was performed using a combination of automatic masking, cycle-variant local RMS thresholding, and manual masking to limit artefacts around bright sources. The final images were obtained with a final deconvolution without the manual mask. The images shown in this paper are not primary beam corrected. Primary beam-corrected images were generated using the DDFacet package (Tasse et al. 2018) and used for the analysis reported in Section 4. We imaged out to an extent of $\sim 1^\circ$ in diameter using 19 × 19 facets for which the rms noise is within 80 per cent of the central noise level at the top of the bandwidth. The antenna response used in this patch-wise correction is smoothed from holographic measurements carried out at the *L* band (Asad et al. 2019).

3 OPTICAL DATA

We used *Subaru*-SuprimeCam images to identify optical counterparts of the MeerKAT radio sources. The Suprime stacked images for MACS J1931.8−2634 in the *B*, *V*, *Rc*, *Ic*, and *z* filters were retrieved from the STScI CLASH data products.[4] On the other hand, the images for A 1300 were created from our own data reduction of the raw *Subaru*-SuprimeCam images in the g' and r' bands retrieved from the SMOKA-Subaru Archive[5] obtained for the MCC, and from the ESO Archive (WFI images B, V, Rc, Programme 084.A-9001). We used the same methods that were used to create the *B*, *V*, *Rc*, *Ic*, *z* Suprime images for MACS J1931.8−2634 (e.g. Nonino et al. 2009). Both data sets were photometrically calibrated using matched point-like sources from PanStarr (Chambers et al. 2016), accounting for colour terms. Details of the optical observations are given in Tables 2 and 3 for MACS J1931.8−2634 and A 1300, respectively.

[4] https://archive.stsci.edu/prepds/clash/
[5] https://smoka.nao.ac.jp/index.jsp, http://mergingclustercollaboration.org/

Downloaded from https://academic.oup.com/mnras/article/504/2/2924/6219094 by CNR BOLOGNA AREA DELLA RICERCA user on 17 March 2022

Table 2. MACSJ1931.8−2634 optical observations.

(1) Observation date	(2) Filter	(3) Exposure (s)	(4) FWHM (arcsec)	(5) Depth[a]
2006 and 2012	*B*	2640	1.20	25.98
2006	*V*	1275	0.88	25.33
2006 and 2012	*Rc*	4560	0.81	25.18
2006	*Ic*	1800	0.92	24.7
2012	*z*	1950	0.76	24.42

[a]Depth: AB magnitude 5σ in 2-arcsec-diameter aperture.

Table 3. A1300 optical observations.

(1) Observation date	(2) Filter	(3) Exposure (s)	(4) FWHM (arcsec)	(5) Depth[a]
2014	g'	720	1.06	25.69
2014	r'	2880	0.94	26.17

[a]Depth: AB magnitude 5σ in 2-arcsec-diameter aperture.

All magnitudes are in the AB system.

For each cluster, the galaxy catalogues were then generated, and the magnitudes were corrected for galactic extinction according to Schlafly & Finkbeiner (2011). The filter sets for the two clusters were not the same; in particular, the two *r*-band throughputs are slightly different: Using spectral energy distribution (SED) fitting of galaxies that are optical counterparts of radio sources (see Section 4.3), the difference r'–Rc ranges from ≈0.1 to ≈0.16 for blue and red galaxies, respectively, at $z \approx 0.30$–0.35, i.e. at the cluster redshift.

4 RESULTS AND DISCUSSION

The $1^\circ \times 1^\circ$ MeerKAT images are shown in Figs 2 and 3. An average rms noise of 40 μJy beam^{-1} is achieved on both targets. The image quality is generally good, although affected by some residual stripes likely due to low-level residual RFI that were not entirely removed despite the multiple flagging process. A couple of bright, off-axis sources are affected by calibration errors that would require direction-dependent calibration. As they do not impact the goals of the current analysis, we leave this to a future work.

Despite the inadequate resolution of our images and the limitations in the *uv* coverage, the giant radio halo in A 1300 and the radio relic are visible in the inner region of the field shown in Fig. 2. A few strong sources are distributed over the whole field of view, which is otherwise populated by faint radio sources. Fig. 3 shows that the field of MACS J1931.8−2634 is dominated by faint radio sources, too. Radio–optical overlays of the central 5.5 arcmin × 5.5 arcmin region are displayed in Fig. 4 for both clusters.

The A 1300 radio galaxies (Fig. 4, left-hand panel) are labelled according to Reid et al. (1999). At the resolution and sensitivity of our images, the BCG is associated with a compact radio source, while A2 is most likely a tailed radio galaxy. Considering the slightly different observing frequencies, the flux densities of the sources labelled in Fig. 4 (left-hand panel) are consistent with those in Reid et al. (1999) within the errors. The relic is very clearly imaged, and consistent in size with the 325 MHz image in Venturi et al. (2013).

The central region of MACS J1931.8−2634 (Fig. 4, right-hand panel) is dominated by the radio emission associated with the BCG and the NAT galaxy. At the angular resolution and sensitivity of our image, the morphology of the BCG is fully consistent with the 1.4 GHz VLA–B image reported in Giacintucci et al. (2014); i.e. no further emission is detected surrounding the BCG. The total flux density of the radio emission in our image is 53 ± 1 mJy, slightly lower than that reported at 1.4 GHz by Giacintucci et al. (2014), i.e. $S_{1.4\,\mathrm{GHz}} = 62 \pm 3$ mJy (see also Ehlert et al. 2011). The overall morphology and extent of the NAT are very similar to those shown in Giacintucci et al. (2014).

4.1 Source extraction

For both clusters, we extracted the radio sources using the `PyBDSF` (Mohan & Rafferty 2015) package from the images not corrected for the primary beam, where the noise is fairly flat over the whole field. `PyBDSF` first estimates a noise map by calculating the rms noise over a 16-pixel box sliding by a 50-pixel window. Following Williams et al. (2016), the box was taken about two times smaller around bright sources to account for the possible local noise increase due to calibration artefacts. The sources were extracted by first identifying islands of contiguous emission above a given threshold, and then decomposing islands into Gaussian components. A threshold of five and four times the local rms noise was used to define sources and island boundaries, respectively. The flux density of the sources was then corrected for primary beam attenuation. We detected 107 and 162 radio sources within the inner 30 arcmin in the field of A 1300 and MACS J1931.8−2634, respectively, above the threshold of 5σ (0.2 mJy) in the images not corrected for the primary beam attenuation. Most of the sources detected in both fields are unresolved or barely resolved. We assume that a radio source is resolved when its deconvolved major and minor axes, as given by PyBDSF, are larger than the restoring beam of the image. The radio source catalogues are reported in Tables A1 and A2.

We tested the accuracy of our flux density calibration by comparing our catalogue with the NVSS catalogue (Condon et al. 1998). We first produced MeerKAT images matching the NVSS 45 arcsec angular resolution, and used them to fit for the flux density for those sources that we considered isolated (i.e. not blended with other sources) and compact (to account for the different angular resolution and *uv* coverage of MeerKAT–16 and NVSS) within 30 arcmin from the pointing centre. We finally scaled the MeerKAT flux density to 1.4 GHz (NVSS observing frequency) assuming a spectral index[6] $\alpha = 0.7$ for all the sources. This procedure ensures a one-to-one match between the two catalogues. The result of our comparison is reported in Fig. 5. Although there is some scatter below 10 mJy, the alignment between the two measurements is generally good and the rms of the relative difference is ∼16 per cent for sources brighter than 8 mJy at 1.28 GHz, which is most likely due to the higher sensitivity of NVSS to extended emission. We consider this number as an indication of the accuracy of our absolute flux density scale. The errors on the flux density measurements reported in Tables A1 and A2 are the PyBDSF fit errors that do not include the uncertainty on the flux density scale.

4.2 Radio source counts

As a first step to test possible differences in the radio source population, after primary beam correction we derived the differential radio source counts in a circular area of radius $r = 12$ arcmin. We chose the same area (0.125 deg^2), which corresponds to about two

[6]We used the convention $S_\nu \propto \nu^{-\alpha}$, where S_ν is the flux density at the frequency ν.

Downloaded from https://academic.oup.com/mnras/article/504/2/2924/6219094 by CNR BOLOGNA AREA DELLA RICERCA user on 17 March 2022

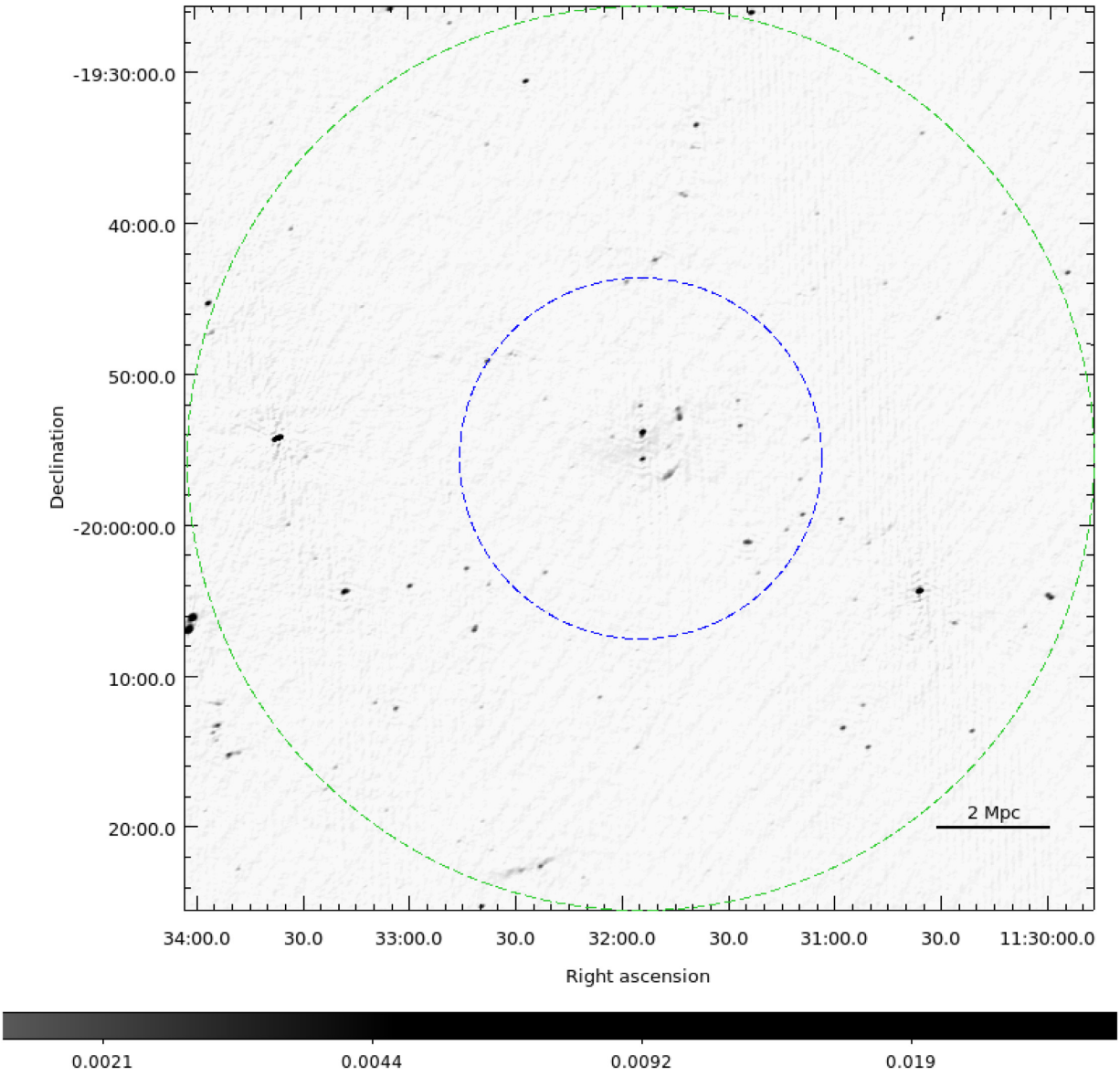

Figure 2. Greyscale image of the galaxy cluster A 1300 and its field at 1.28 GHz. The green dashed circle has an ∼1 deg diameter and represents the HPBW of the MeerKAT primary beam. This is the area used to extract the source catalogue. The blue dashed circle marks the inner 12 arcmin radius (i.e. 0.125 deg^2 area), corresponding to about two virial radii. The angular resolution is 12 arcsec × 5 arcsec. Units are Jy beam^{-1}.

virial radii in both clusters (blue dashed circle in Figs 2 and 3). We expect that the cluster dynamics may not impact the radio emission of individual galaxies beyond this distance.

To account for the different angular resolution of the final images of the two cluster fields (see Table 1) and ensure a homogeneous analysis, we generated an image of the MACS J1931.8−2634 field with a 12 arcsec × 5 arcsec restoring beam, and used this latter image in the following steps.

To derive the contribution of the two clusters to the differential source counts, we estimated the background source counts from the annular region between the blue and green circles (30 arcmin) in Fig. 2 and in the 12 arcsec × 5 arcsec image of MACS J1931.8−2634, which corresponds to a 0.66 deg^2 area. Figs 6 and 7 show the differential source counts N for the 0.125 deg^2 area centred on the two clusters and the background (0.66 deg^2), respectively. The background counts were not subtracted from 0.125 deg^2 central area. The source counts have been normalized to 1 square deg in both figures.

The source count distributions tend to decline below ∼0.5 mJy, corresponding to 10σ (dashed line in Figs 6 and 7). We interpret such decline as an indication of the completeness limit of our samples, partly due to the primary beam attenuation, which is ∼20 per cent at 30 arcmin and negligible at 12 arcmin. Since our analysis is carried out on images with the same angular resolution, at the same frequencies and, therefore, with the same primary beam, this implies that the completeness is the same for both cases. For the purpose of our relative comparison, the estimate and correction of completeness are therefore not necessary.

We performed a two-sample Kolmogorov–Smirnov (KS) test between the A 1300 and MACS J1931.8−2634 using the source catalogues extracted in their central area (12 arcmin radius). The test yielded a 0.05 p-value, implying that we can reject the null

Downloaded from https://academic.oup.com/mnras/article/504/2/2924/6219094 by CNR BOLOGNA AREA DELLA RICERCA user on 17 March 2022

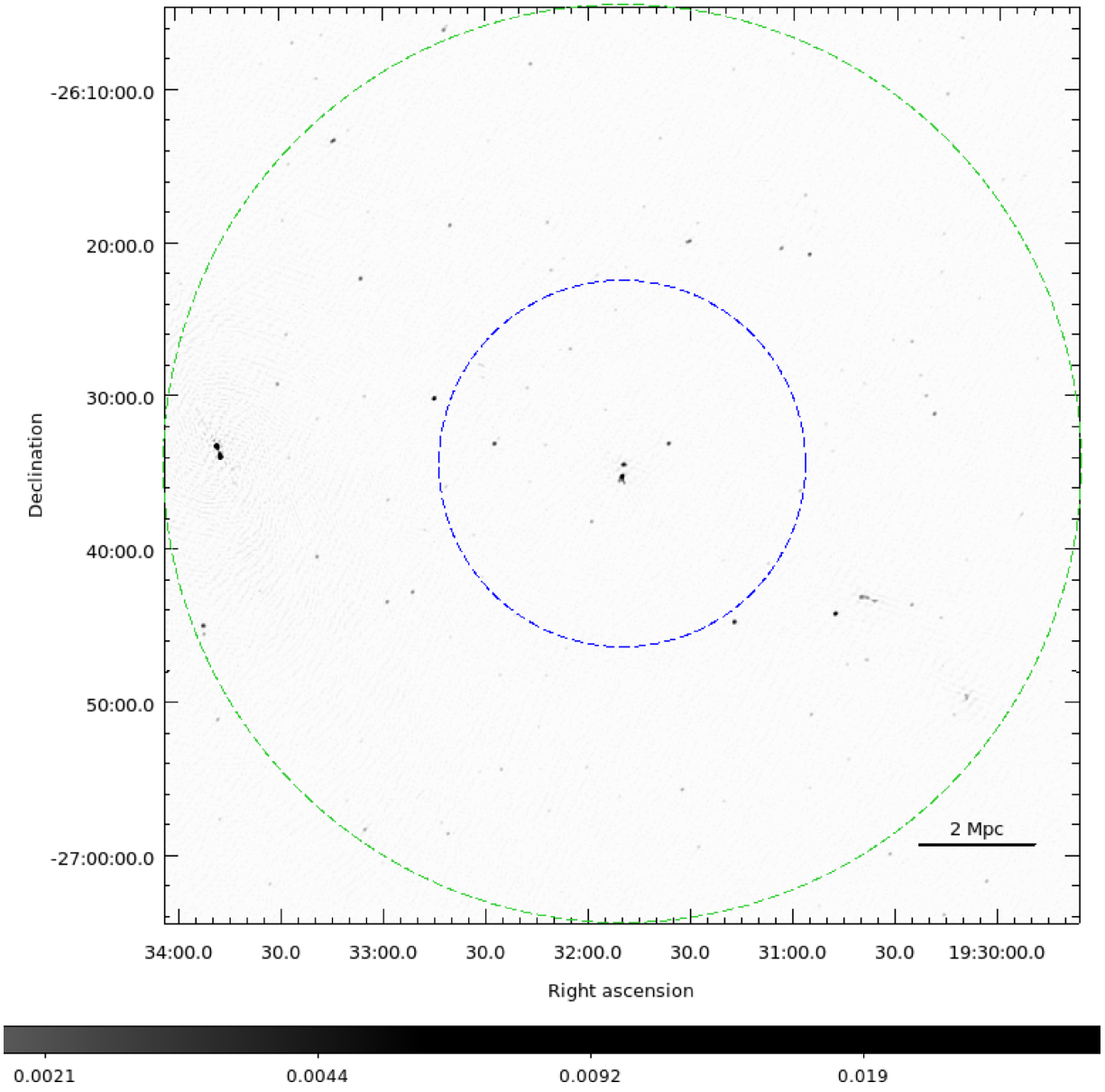

Figure 3. Same as Fig. 2, but for the MACS J1931.8−2634 galaxy cluster and its field. The angular resolution is 5 arcsec × 3 arcsec.

hypothesis that the radio source catalogues are drawn from the same distribution with a 95 per cent significance. The two distributions for the background source counts are in very good agreement with each other, except for the first two bins at low flux densities.

4.3 Optical identifications

To search for optical counterparts, we used the *Rc* band for MACS J1931.8−2634 and the r' band for A 1300, the image quality being better since both filters lie redward of the 4000 Å break. We carried out the optical identifications of radio sources in our catalogues within about two virial radii by cross-correlating their positions with the catalogues derived from the *Subaru*-SuprimeCam images (see Section 3). As the primary beam correction is negligible out to this distance from the pointing centre, our optical identifications are complete at the 0.2 mJy flux density level.

The optical position error is $\sigma_{\rm o} \sim 0.02$ arcsec. We estimated the radio position error $\sigma_{\rm r}$ as (Prandoni et al. 2000)

$$\sigma_{\rm r} = \frac{\theta_{\rm s}}{2\,{\rm SNR}}, \quad (1)$$

where $\theta_{\rm s}$ is the synthesized beam size (Table 1) and SNR is the signal-to-noise ratio. For the faintest sources (SNR $= 5\sigma$), $\sigma_{\rm r} = 1.2$ and 0.5 arcsec for A 1300 and MACS J1931.8−2634, respectively. The matching criterion was based on the R parameter defined as (Giacintucci et al. 2004)

$$R^2 = \frac{\Delta^2_{\rm r-o}}{\sigma^2_{\rm r} + \sigma^2_{\rm o}}, \quad (2)$$

where $\Delta_{\rm r-o}$ is the radio–optical position offset. We considered reliable identifications all the nearest neighbour matches with $R \leq 3$. After further visual inspection, we were left with 26 optical counterparts in the A 1300 cluster field (∼24 per cent of the total number of radio sources), and 25 optical counterparts in the

Downloaded from https://academic.oup.com/mnras/article/504/2/2924/6219094 by CNR BOLOGNA AREA DELLA RICERCA user on 17 March 2022

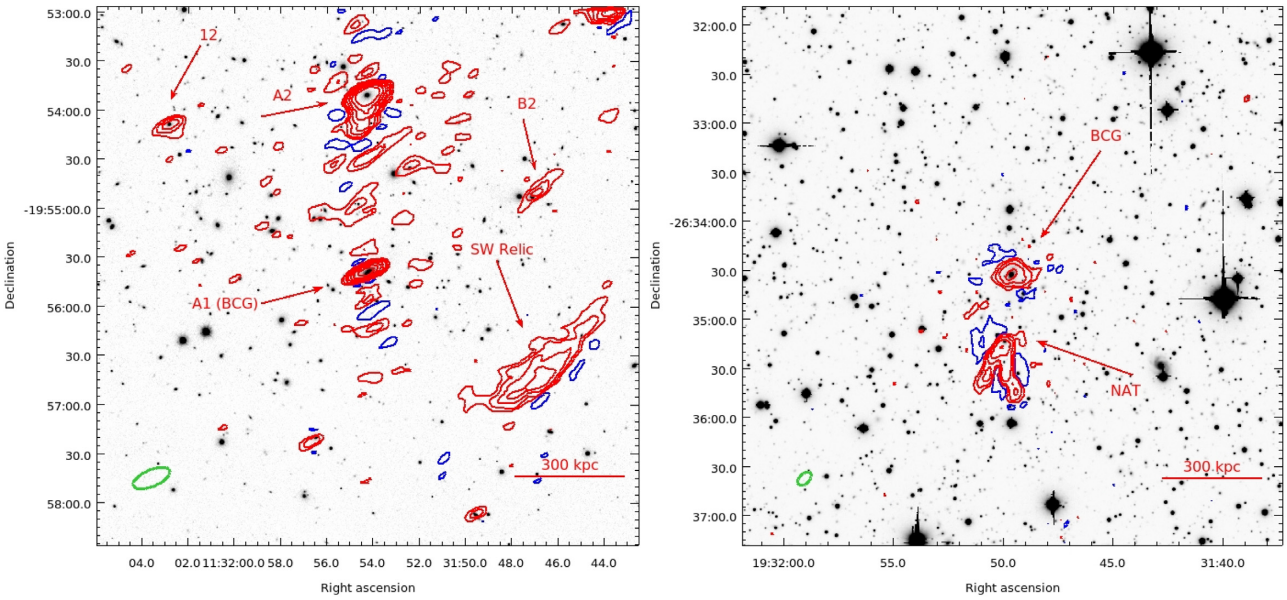

Figure 4. Left-hand panel: A 1300 radio contours (red) overlaid on the greyscale infrared band image (K_s band from GCAV). Radio contours start at 3σ (1σ = 0.04 mJy beam^{-1}) and then scaled by a factor of 2. The first negative contour (-3σ level) is drawn in blue. Galaxies are labelled following Reid et al. (1999). Right-hand panel: same as left-hand panel but for MACS J1931.8−2634. Radio contours are overlaid on the optical Suprime image (*Ic* filter). The restoring beam for each image is shown as a green ellipse in the bottom left corner in both panels.

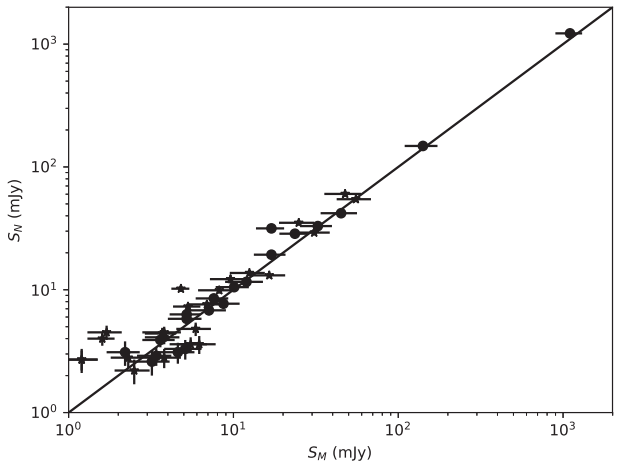

Figure 5. Comparison between the NVSS flux density S_N and the MeerKAT flux density S_M scaled at 1.4 GHz assuming a spectral index $\alpha = 0.7$ for sources common to both cluster catalogues within a 30 arcmin radius from the image centre.

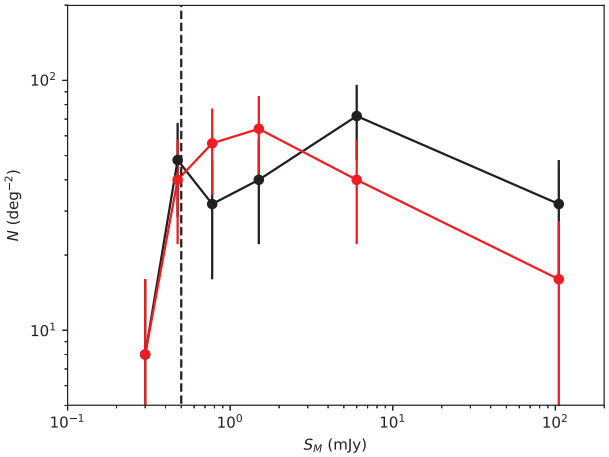

Figure 6. Differential radio source counts in A 1300 (black) and MACS J1931.8−2634 (red) at 1.28 GHz in the central 0.125 deg^2 area, corresponding to two virial radii (blue dashed circle in Figs 2 and 3).

MACS J1931.8−2634 cluster field (∼15 per cent of the total number of radio sources).

The information on the optical counterparts was complemented with the redshift data to identify cluster members.

In A 1300, the redshift information was taken from Ziparo et al. (2012).[7] We retrieved and re-analysed the VIMOS spectroscopic data in Ziparo et al. (2012), limiting to slit including optical counterparts of radio sources and to targets with r' brighter than 20.4 (see Table 4). Combining our re-analysis with information from NED, we found 14 spectroscopic redshifts, 9 of which are consistent with being cluster members. Among these nine galaxies, four are new findings from our re-analysis.

For MACS J1931.8−2634, the redshift information was obtained from Rosati et al. (2014, private communication).[8] We found eight spectroscopic redshifts, six of which are consistent with being cluster members.

Even though we did not perform a full pseudo-phase space analysis, using the rest frame $\Delta(v - v_{\rm cluster})$ and the projected distance from the BCG, assumed to be the centre of the cluster, both clusters show that the optical counterparts with spectroscopic redshift lie within the phase-space diagram that envelops the cluster members (fig. 4 in Ziparo et al. 2012). Since the two clusters have similar mass, the phase-space diagram for the two clusters is similar, and this has been confirmed from a preliminary analysis of the yet unpublished CLASH-VLT data of MACS J1931.8−2634. This confirms that the

[7]ESO GO Large Programme, PI Böringer, ID number 169.A–0595.

[8]CLASH VLT-ESO Large Programme, PI Rosati, ID number 186.A-0798.

Downloaded from https://academic.oup.com/mnras/article/504/2/2924/6219094 by CNR BOLOGNA AREA DELLA RICERCA user on 17 March 2022

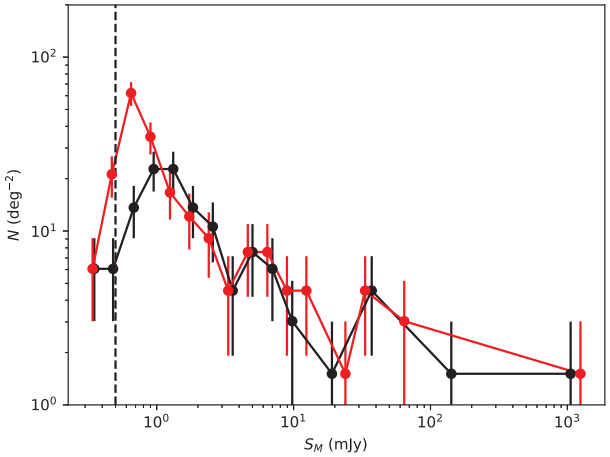

Figure 7. Same as Fig. 6, but for the background (the 0.66 deg^2 area between the blue and the green circles in Figs 2 and 3).

radio galaxies with spectroscopic redshift counterparts in the range of 0.29–0.31 and 0.34–0.36 for A 1300 and MACS J1931.8−2634, respectively, are most likely cluster members.

The full list of optical identifications is given in Tables B1 and B2, and the radio–optical details of the cluster members are given in Table 4.

Although beyond the scope of this paper, it is worth noting that using SED fitting (MAGPHYS; da Cunha, Charlot & Elbaz 2008) both in A 1300 and in MACS J1931.8−2634 the cluster radio galaxies split into quiescent and star forming with respect to the specific star formation rate, which reflects the blue and red colours in the colour–magnitude diagrams (not shown here).

4.4 The RLF

The RLF is a solid statistical tool to investigate the radio properties of a galaxy population (Ledlow & Owen 1996; Venturi et al. 2000; Giacintucci et al. 2004; Branchesi et al. 2006). To further explore if and how the dynamical properties of galaxy clusters affect the statistical properties of the radio galaxy population, we derived the RLF in both clusters. In particular, the influence of the environment should be reflected in the shape of the RLF or in its amplitude, or both.

Consistent with the radio source counts, our analysis has been carried out within about two virial radii (12 arcmin) in both clusters. The 1.28 GHz k-corrected radio power of the cluster radio galaxies ranges from $22.95 < \log P_{1.28\,\mathrm{GHz}}\,(\mathrm{W\,Hz^{-1}}) < 25.03$ in A 1300 and $22.98 < \log P_{1.28\,\mathrm{GHz}}\,(\mathrm{W\,Hz^{-1}}) < 25.31$ in MAC J1931.8−2643 (see Table 4). The redshift of the individual galaxies was used to evaluate the k-correction. We divided this interval into bins of $\Delta\log P = 0.4$ in A 1300. Due to the lower number of sources, we chose a bin width of $\Delta\log P = 0.6$ for MACS J1931.8−2634.

To ensure optical completeness in the normalization of the radio galaxy distribution, we selected all the galaxies in the magnitude range of $18.6 < m_{r'} < 20.3$ for A 1300 and those in the magnitude range of $18.1 < m_{\mathrm{Rc}} < 19.7$ for MACS J1931.8–2634. The negligible impact of the different filters for the two clusters is discussed in Section 3. The faint limits in r' and Rc are approximately 5 mag brighter than the depth of the stacked images, which ensures completeness of the optical samples in both clusters. We used the r' and Rc filters that are redder than the 4000 Å break for both clusters, and they have similar system transmission as opposed to the g and B, V filters.

We obtained 261 objects for A 1300, 70 of which have spectroscopic redshift in the range of $0.29 < z_{\mathrm{sp}} < 0.31$, and 1181 objects for MACS J1931.8−2634, 220 of which have spectroscopic redshift in the $0.34 < z_{\mathrm{sp}} < 0.36$ range. Each radio power bin has been normalized by 70 and 220, respectively, for A 1300 and MACS J1931.8−2634, as clear from Table 5, which reports the radio power interval (Col. 1) and the values of the fractional and integral RLF (Col. 2 and Col. 3, respectively) for both clusters. MACS J1931.8−2634 is reported in the upper part of the table, and A 1300 in the lower part. The two integral RLFs are shown in Fig. 8.

The integral RLF has a similar slope in both clusters, the one in A 1300 being systematically higher compared to MACS J1931.8−2634 one. Unfortunately, the samples are not large enough to perform a KS test, and we integrated the RFLs in

Table 4. Details of the cluster members. Left to right: (1) radio source name; (2) and (3) J2000 right ascension and declination; (4) flux density at 1.28 MHz S_{M}; (5) indication on source size (extended or not); (6) k-corrected radio power $\mathrm{P}_{1.28\,\mathrm{GHz}}$; (7) and (8) J2000 right ascension and declination of the optical counterpart; (9), (10), and (11) magnitudes and corresponding colours; (12) spectroscopic redshift z_{sp}.

(1) Name	(2) RA_{J2000} (h m s)	(3) $\mathrm{Dec.}_{J2000}$ (° ′ ″)	(4) S_{M} (mJy)	(5) Resolved	(6) $\log P_{1.28\,\mathrm{GHz}}$ (W Hz^{-1})	(7) $\mathrm{RA}_{\mathrm{opt}}$ (h m s)	(8) $\mathrm{Dec.}_{\mathrm{opt}}$ (° ′ ″)	(9) B	(10) Rc	(11) $(B-Rc)$	(12) z_{sp}
J1931−2637	19:31:46.60	−26:37:31.7	0.39 ± 0.04	N	23.22	19:31:46.53	−26:37:31.0	21.95	19.67	2.28	0.342
J1931−2634	19:31:49.58	−26:34:32.7	45.40 ± 0.80	Y–BCG	25.31	19:31:49.63	−26:34:32.6	18.84	18.14	0.70	0.352
J1931−2635	19:31:50.02	−26:35:17.2	145.20 ± 0.70	Y–NAT	25.81	19:31:50.00	−26:35:17.1	21.50	19.20	2.30	0.351
J1931−2630b	19:31:54.86	−26:30:57.7	0.88 ± 0.10	N	23.60	19:31:54.86	−26:30:57.0	21.66	19.46	2.20	0.351
J1931−2645	19:31:58.33	−26:45:34.4	0.25 ± 0.05	N	22.98	19:31:58.32	−26:45:34.4	20.85	19.33	1.52	0.359
J1932−2625	19:32:07.42	−26:25:16.3	0.25 ± 0.05	N	22.98	19:32:07.45	−26:25:16.5	20.52	19.22	1.30	0.349
(1) Name	(2) RA_{J2000} (h m s)	(3) $\mathrm{Dec.}_{J2000}$ (° ′ ″)	(4) S_{M} (mJy)	(5) Resolved	(6) $\log P_{1.28\,\mathrm{GHz}}$ (W Hz^{-1})	(7) $\mathrm{RA}_{\mathrm{opt}}$ (h m s)	(8) $\mathrm{Dec.}_{\mathrm{opt}}$ (° ′ ″)	(9) g'	(10) r'	(11) $(g'-r')$	(12) z_{sp}
J1131−2000	11:31:13.74	−20:00:20.5	1.69 ± 0.17	N	23.73	11:31:13.73	−20:00:21.5	21.35	19.95	1.40	0.303
J1131−1954	11:31:46.79	−19:54:52.5	0.25 ± 0.05	N (B2)	22.89	11:31:47.13	−19:54:52.7	21.05	19.63	1.41	0.302
J1131−1949	11:31:48.62	−19:49:01.7	0.25 ± 0.05	N	22.89	11:31:48.56	−19:49:02.2	21.23	20.21	1.02	0.302
J1131−1958	11:31:49.50	−19:58:07.9	0.39 ± 0.05	N	23.08	11:31:49.53	−19:58:07.6	20.87	19.74	1.13	0.295
J1131−1953b	11:31:54.30	−19:53:53.5	37.80 ± 0.40	Y–TAIL (A2)	25.03	11:31:54.27	−19:53:50.8	20.86	19.41	1.45	0.305
J1131−1955	11:31:54.34	−19:55:39.0	12.10 ± 0.20	Y–BCG (A1)	24.53	11:31:54.18	−19:55:39.8	20.09	18.62	1.46	0.307
J1131−1952b	11:31:54.85	−19:52:07.7	2.30 ± 0.20	Y (A3)	23.80	11:31:54.95	−19:52:10.2	20.70	19.24	1.45	0.303
J1132−1954	11:32:02.77	−19:54:09.0	1.02 ± 0.10	Y (12)	23.38	11:32:02.70	−19:54:13.5	21.23	19.78	1.44	0.306
J1132−1952	11:32:04.16	−19:52:11.1	0.25 ± 0.05	N	22.89	11:32:04.39	−19:52:12.4	21.14	20.39	0.75	0.302

Downloaded from https://academic.oup.com/mnras/article/504/2/2924/6219094 by CNR BOLOGNA AREA DELLA RICERCA user on 17 March 2022

Table 5. RLFs of MACS J1931.8−2634 (top part) and A 1300 (bottom part) clusters, respectively. From left to right: radio power (logarithmic) interval, differential RLF (normalized by the number of cluster optical galaxies), and cumulative RLF.

(1) $\Delta\log P_{1.28\,\mathrm{GHz}}$	(2) Differential RLF	(3) Integral RLF
22.95–23.55	3/220	0.0271
23.55–24.15	1/220	0.0135
24.15–24.75	0/220	0.009
24.75–25.35	1/220	0.009
25.35–25.95	1/220	0.0045
22.81–23.21	4/70	0.1284
23.21–23.61	1/70	0.0713
23.61–24.01	2/70	0.0571
24.01–24.41	0/70	0.0285
24.41–24.81	1/70	0.0285
24.81–25.21	1/70	0.0142

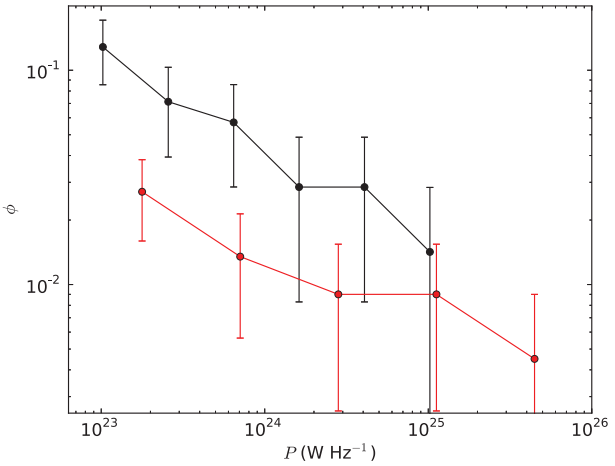

Figure 8. Integral RLF of the A 1300 (black) and MACS J1931.8−2634 (red) cluster, respectively (see the text for details).

a single power bin over the full radio power range. In order to account for the different radio power detection limit in the two clusters ($\log P_{1.28\,\mathrm{GHz}} = 22.89$ and 22.98 for A 1300 and MACS J1931.8−2634, respectively), we removed the three objects with $\log P_{1.28\,\mathrm{GHz}} = 22.89$ in A 1300. We obtained 0.027 ± 0.011 for MACS J1931.8−2634 and 0.09 ± 0.04 for A 1300, respectively, leading to a 3.3 ± 1.9 ratio between the two integral RFLs. These results indicate that the evidence of enhanced radio emission in A 1300 is negligible (1.2σ).

5 SUMMARY AND FUTURE WORK

In this paper, we presented new 1.28 GHz MeerKAT observations of the two galaxy clusters A 1300 and MACS J1931.8−2634 as part of the MeerKAT early science programme, when only 16 antennas were available for observing. Observations served to test calibration and imaging pipelines for MeerKAT. As scientific goal, we selected a merging cluster (A 1300) and a relaxed cluster (MACS J 1931.8−2634) with similar mass located at $z \sim 0.3$ in order to isolate effects due to cosmological evolution, for a comparative study of the properties of the radio galaxy population in different environments. A 1300 is a merging cluster, with a well-studied giant radio halo and a relic, as often found in merging clusters; MACS J1931.8−2634 is a relaxed cluster hosting one of the most X-ray luminous cool cores, and extended emission of unclear nature surrounding the radio AGN associated with the BCG.

The angular resolution and *uv* coverage of our observations are very well suited to perform a comparative study of the statistical properties of the radio galaxy population, which we carried out by means of the radio source counts and the RLF.

We extracted a radio source catalogue for each cluster down to a 0.2 mJy threshold (corresponding to 5σ) and out to about two virial radii (corresponding to a 12 arcmin radius) that we consider the extent of the possible effects of cluster dynamics on the radio galaxy population. We further extracted another catalogue from the outskirts of each cluster in an annular area of radius $12 < r < 30$ arcmin, representative of the background distribution.

We performed a two-sample KS test of the radio source counts in the two clusters. We rejected the hypothesis that the cluster catalogues come from the same distribution at a limited, 95 per cent significance.

To further investigate if and how the cluster dynamics affects the radio emission of cluster galaxies, we complemented our radio catalogues with optical data in order to derive the radio–optical luminosity function for each cluster. In particular, we used *Subaru* SuprimeCam data for A 1300 in the g' and r' and the CLASH full filter coverage for MACS J1931.8−2634. These datasets are ≈5 mag deeper than the faint limits used for the radio–optical luminosity function. The optical data were complemented with redshift information from the literature, yielding to the identification of 9 cluster radio galaxies out to 70 cluster members and 6 cluster radio galaxies out of 220 cluster members in A 1300 and MACS J1931.8−2634, respectively. These radio galaxies were used to compute the differential and integral RLFs that span the power range of $22.81 < \log P_{1.28\,\mathrm{GHz}}\,(\mathrm{W\,Hz^{-1}}) < 25.95$.

We found that the integral RLF in A 1300 systematically lies above the MACS J1931.8−2634 one. After averaging over the whole common power interval, the ratio of the two RLFs is 3.3 ± 1.9, implying that the probability to host radio emission is 3.3 times higher in A 1300. Due to the small sample, however, this result is not statistically significant (1.2σ level), suggesting that the role of cluster mergers as a trigger of radio emission in the cluster galaxy population is negligible.

The analysis presented in this work, though limited by the small statistics, aligns with the previous studies in the field, and the role of cluster dynamics on the global statistical properties of radio galaxies remains unclear (see Ledlow & Owen 1996; Venturi et al. 2000; Giacintucci et al. 2004). Future, more sensitive observations with the full MeerKAT array will increase the sample statistics and allow a more robust confirmation of the findings presented here.

ACKNOWLEDGEMENTS

The MeerKAT telescope is operated by the South African Radio Astronomy Observatory, which is a facility of the National Research Foundation, an agency of the Department of Science and Innovation. This work is based on research supported in part by the National Research Foundation of South Africa (grant number 103424). We acknowledge the support from the Ministero degli Affari Esteri e della Cooperazione Internazionale, Direzione Generale per la Promozione del Sistema Paese, Progetto di Grande Rilevanza ZA18GR02. Based in part on data collected at Subaru Telescope and obtained from the Subaru-Mitaka-Okayama-Kiso-Archive (SMOKA), which is operated by the Astronomy Data Center, National Astronomical Observatory of Japan. Basic research in radio astronomy at the Naval Research Laboratory is supported by 6.1 Base funding. Ruta Kale

Downloaded from https://academic.oup.com/mnras/article/504/2/2924/6219094 by CNR BOLOGNA AREA DELLA RICERCA user on 17 March 2022

acknowledges the support of the Department of Atomic Energy, Government of India, under project no. 12-R&D-TFR-5.02-0700.

DATA AVAILABILITY

The data underlying this article will be shared on reasonable request to the corresponding author.

REFERENCES

Abell G. O., Corwin Harold G. J., Olowin R. P., 1989, ApJS, 70, 1
Allen S. W., Schmidt R. W., Ebeling H., Fabian A. C., van Speybroeck L., 2004, MNRAS, 353, 457
Andreon S., Hurn M. A., 2010, MNRAS, 404, 1922
Asad K. M. B. et al., 2019, MNRAS, 502, 2970
Botteon A., Gastaldello F., Brunetti G., Dallacasa D., 2016, Galaxies, 4, 68
Branchesi M., Gioia I. M., Fanti C., Fanti R., Perley R., 2006, A&A, 446, 97
Briggs D. S., 1995, American Astronomical Society Meeting Abstracts, #112.02
Brüggen M., Bykov A., Ryu D., Röttgering H., 2012, Space Sci. Rev., 166, 187
Brunetti G., Jones T. W., 2014, Int. J. Mod. Phys. D, 23, 1430007
Camilo F. et al., 2018, ApJ, 856, 180
Carlberg R. G., Yee H. K. C., Ellingson E., 1997, ApJ, 478, 462
Chambers K. C. et al., 2016, preprint (arXiv:1612.05560)
Condon J. J., Cotton W. D., Greisen E. W., Yin Q. F., Perley R. A., Taylor G. B., Broderick J. J., 1998, AJ, 115, 1693
da Cunha E., Charlot S., Elbaz D., 2008, MNRAS, 388, 1575
Donahue M. et al., 2015, ApJ, 805, 177
Dwarakanath K. S., Owen F. N., 1999, AJ, 118, 625
Ebeling H., 2007, A Snapshot Survey of The Most Massive Clusters of Galaxies, *HST* Proposal
Ebeling H., Edge A. C., Mantz A., Barrett E., Henry J. P., Ma C. J., van Speybroeck L., 2010, MNRAS, 407, 83
Ehlert S. et al., 2011, MNRAS, 411, 1641
Feretti L., Venturi T., 2002, in Feretti L., Gioia I. M., Giovannini G., eds, Radio Galaxies and Their Environment. Kluwer Acad. Publishers, Dordrecht, p. 163
Fogarty K., Postman M., Connor T., Donahue M., Moustakas J., 2015, ApJ, 813, 117
Giacintucci S., Venturi T., Bardelli S., Dallacasa D., Zucca E., 2004, A&A, 419, 71
Giacintucci S., Markevitch M., Venturi T., Clarke T. E., Cassano R., Mazzotta P., 2014, ApJ, 781, 9
Giacintucci S., Markevitch M., Cassano R., Venturi T., Clarke T. E., Brunetti G., 2017, ApJ, 841, 71
Gralla M. B., Gladders M. D., Yee H. K. C., Barrientos L. F., 2011, ApJ, 734, 103
Jonas J., MeerKAT Team, 2016, Proc. Sci., The MeerKAT Radio Telescope. SISSA, Trieste, PoS#1
Kale R., Venturi T., Cassano R., Giacintucci S., Bardelli S., Dallacasa D., Zucca E., 2015, A&A, 581, A23
Kenyon J. S., Smirnov O. M., Grobler T. L., Perkins S. J., 2018, MNRAS, 478, 2399
Ledlow M. J., Owen F. N., 1996, AJ, 112, 9
Lemonon L., Pierre M., Hunstead R., Reid A., Mellier Y., Boehringer H., 1997, A&A, 326, 34
McMullin J. P., Waters B., Schiebel D., Young W., Golap K., 2007, in Richard A. S., Frank H., David J. B., eds, ASP Conf. Ser. Vol. 376, Astronomical Data Analysis Software and Systems XVI. Astron. Soc. Pac., San Francisco, p. 127
Makhathini S., 2018, PhD thesis, Rhodes Univ., Drosty Rd, Grahamstown, Eastern Cape, South Africa, p. 6139
Mauch T., Sadler E. M., 2007, MNRAS, 375, 931
Mauch T. et al., 2020, ApJ, 888, 61
Melchior P. et al., 2017, MNRAS, 469, 4899
Merten J. et al., 2015, ApJ, 806, 4
Miller N. A., Owen F. N., 2003, AJ, 125, 2427
Mittal R., Hudson D. S., Reiprich T. H., Clarke T., 2009, A&A, 501, 835
Mohan N., Rafferty D., 2015, PyBDSF: Python Blob Detection and Source Finder, Astrophysics Source Code Library, record ascl:1502.007
Nonino M. et al., 2009, ApJS, 183, 244
Offringa A. R., van de Gronde J. J., Roerdink J. B. T. M., 2012, A&A, 539, A95
Offringa A. R. et al., 2013, A&A, 549, A11
Offringa A. R. et al., 2014, MNRAS, 444, 606
Owen F. N., Ledlow M. J., Keel W. C., Morrison G. E., 1999, AJ, 118, 633
Pierre M. et al., 1994, The Messenger, 78, 24
Pierre M., Oukbir J., Dubreuil D., Soucail G., Sauvageot J. L., Mellier Y., 1997, A&AS, 124, 283
Postman M. et al., 2012, ApJS, 199, 25
Prandoni I., Gregorini L., Parma P., de Ruiter H. R., Vettolani G., Wieringa M. H., Ekers R. D., 2000, A&AS, 146, 41
Press W. H., Schechter P., 1974, ApJ, 187, 425
Reid A. D., Hunstead R. W., Lemonon L., Pierre M. M., 1999, MNRAS, 302, 571
Reynolds J., 1994, ATNF Internal
Rosati P. et al., 2014, The Messenger, 158, 48
Santos J. S. et al., 2016, MNRAS, 456, L99
Sarazin C. L., 2002, The Physics of Cluster Mergers. p. 1
Schlafly E. F., Finkbeiner D. P., 2011, ApJ, 737, 103
Stocke J. T., Perlman E. S., Gioia I. M., Harvanek M., 1999, AJ, 117, 1967
Tasse C. et al., 2018, A&A, 611, A87
Umetsu K. et al., 2014, ApJ, 795, 163
Venturi T., Bardelli S., Morganti R., Hunstead R. W., 2000, MNRAS, 314, 594
Venturi T., Bardelli S., Zambelli G., Morganti R., Hunstead R. W., 2001, MNRAS, 324, 1131
Venturi T., Giacintucci S., Dallacasa D., Cassano R., Brunetti G., Macario G., Athreya R., 2013, A&A, 551, A24
Williams W. L. et al., 2016, MNRAS, 460, 2385
Ziparo F., Braglia F. G., Pierini D., Finoguenov A., B'ohringer H., Bongiorno A., 2012, MNRAS, 420, 2480

APPENDIX A: RADIO SOURCE CATALOGUES

We provide the radio catalogues for A 1300 (Table A1) and MACS J1931.8−2634 (Table A2) fields extracted within 30 arcmin radius from the pointing centre. The `pyBDSF` fitted positions and MeerKAT flux densities are also indicated.

Downloaded from https://academic.oup.com/mnras/article/504/2/2924/6219094 by CNR BOLOGNA AREA DELLA RICERCA user on 17 March 2022

Table A1. A 1300 radio source catalogue. The columns report the name of the radio source (Col. 1), J2000 right ascension and declination (Col. 2 and Col. 3, respectively), the total flux density (Col. 4), and a note on the morphology (Col. 5). Radio source names D follow the J HHMM–DDMM nomenclature. All sources with $S_{tot} > S_{peak}$ (where S_{tot} and S_{peak} are the total flux density and peak flux density at 1.28 GHz, respectively) are considered resolved. Cluster members are listed in boldface.

(1) Name	(2) RA_{J2000} (hms)	(3) $Dec._{J2000}$ (° ' ")	(4) $S_{1.28\,GHz}$ (mJy)	(5) Resolved
J1129–1949	11:29:55.82	−19:49:35.7	0.60 ± 0.14	Y
J1129–2004	11:29:59.64	−20:04:44.1	27.00 ± 0.30	Ext. FRII
J1130–1958	11:30:05.08	−19:58:21.9	0.44 ± 0.26	Y
J1130–2006	11:30:06.61	−20:06:44.2	2.07 ± 0.11	Y
J1130–1939	11:30:12.67	−19:39:19.9	1.78 ± 0.18	Y
J1130–2013a	11:30:21.47	−20:13:38.3	6.09 ± 0.12	Y
J1130–1936	11:30:23.66	−19:36:16.6	0.43 ± 0.32	Y
J1130–2009	11:30:28.10	−20:09:27.6	0.74 ± 0.12	Y
J1130–1945	11:30:28.86	−19:45:56.9	0.69 ± 0.23	Y
J1130–1946	11:30:31.16	−19:46:16.2	2.32 ± 0.12	Y
J1130–2007a	11:30:33.01	−20:07:45.0	1.33 ± 0.12	Y
J1130–1934	11:30:35.86	−19:34:01.6	2.53 ± 0.17	Y
J1130–2004a	11:30:36.33	−20:04:23.0	135.1 ± 0.4	Y
J1130–2007b	11:30:38.45	−20:07:35.6	0.27 ± 0.05	Y
J1130–1943	11:30:46.10	−19:43:59.4	1.57 ± 0.10	N
J1130–2001	11:30:50.60	−20:01:12.1	1.35 ± 0.10	Y
J1130–2014	11:30:50.75	−20:14:43.7	5.75 ± 0.09	Y
J1130–2008	11:30:51.71	−20:08:55.4	0.81 ± 0.09	Y
J1130–2011	11:30:52.17	−20:11:56.7	2.58 ± 0.17	Y
J1130–2004b	11:30:54.40	−20:04:58.1	0.97 ± 0.07	Y
J1130–2013b	11:30:57.85	−20:13:27.6	7.85 ± 0.10	Y
J1130–1959	11:30:58.41	−19:59:36.6	2.45 ± 0.08	Y
J1131–1939	11:31:05.15	−19:39:22.6	1.61 ± 0.10	N
J1131–1944a	11:31:06.20	−19:44:23.1	1.13 ± 0.13	Y
J1131–1954	11:31:08.22	−19:54:17.2	1.42 ± 0.15	Y
J1131–1959a	11:31:09.25	−19:59:19.0	4.20 ± 0.08	Y
J1131–1956	11:31:09.94	−19:56:58.0	1.49 ± 0.08	Y
J1131–1944b	11:31:10.21	−19:44:42.5	0.41 ± 0.10	Y
J1131–2000	**11:31:13.74**	**−20:00:20.5**	**1.69 ± 0.11**	**N**
J1131–2019a	11:31:17.81	−20:19:49.2	0.57 ± 0.20	Y
J1131–1952a	11:31:19.48	−19:52:39.7	0.74 ± 0.07	Y
J1131–1946a	11:31:20.85	−19:46:06.7	0.76 ± 0.08	Y
J1131–2003	11:31:21.65	−20:03:11.7	1.47 ± 0.07	N
J1131–2017	11:31:22.36	−20:17:33.8	0.29 ± 0.16	Y
J1131–1947	11:31:22.48	−19:47:31.3	0.47 ± 0.09	Y
J1131–2001	11:31:24.77	−20:01:09.6	10.30 ± 0.10	Y
J1131–1953a	11:31:26.89	−19:53:26.1	3.91 ± 0.08	Y
J1131–1951	11:31:27.51	−19:51:46.1	1.36 ± 0.09	N
J1131–1931	11:31:29.90	−19:31:48.7	1.07 ± 0.11	Y
J1131–1946b	11:31:32.53	−19:46:59.5	0.63 ± 0.07	Y
J1131–2022	11:31:35.60	−20:22:55.3	0.47 ± 0.19	Y
J1131–2007a	11:31:35.76	−20:07:28.7	0.47 ± 0.08	Y
J1131–1933	11:31:39.27	−19:33:29.6	10.40 ± 0.10	Y
J1131–1934	11:31:40.32	−19:34:59.1	1.05 ± 0.12	Y
J1131–2019b	11:31:42.40	−20:19:25.1	1.07 ± 0.14	Y
J1131–1938	11:31:43.46	−19:38:02.8	1.29 ± 0.15	Ext. FRII
J1131–1952	11:31:43.92	−19:52:54.2	16.20 ± 0.10	Ext. (WAT–B1)
J1131–1954	**11:31:46.79**	**−19:54:52.5**	**0.25 ± 0.05**	**N (B2)**
J1131–1950	19:31:48.42	−19:50:43.8	0.70 ± 0.08	N
J1131–1949	**11:31:48.62**	**−19:49:01.7**	**0.25 ± 0.05**	**N**
J1131–1958	**11:31:49.50**	**−19:58:07.9**	**0.39 ± 0.05**	**N**
J1131–1942	11:31:50.85	−19:42:27.1	4.78 ± 0.21	Y
J1131–2012	11:31:53.49	−20:12:11.2	0.67 ± 0.09	Y
J1131–1953b	**11:31:54.30**	**−19:53:53.5**	**37.80 ± 0.40**	**Y–TAIL (A2)**
J1131–1955	**11:31:54.34**	**−19:55:39.0**	**12.10 ± 0.20**	**Y–BCG (A1)**
J1131–1943a	11:31:54.56	−19:43:47.6	0.47 ± 0.20	Y
J1131–1952b	**11:31:54.85**	**−19:52:07.7**	**2.30 ± 0.13**	**Y (A3)**

Downloaded from https://academic.oup.com/mnras/article/504/2/2924/6219094 by CNR BOLOGNA AREA DELLA RICERCA user on 17 March 2022

Table A1 – *continued*

(1) Name	(2) RA_{J2000} (hms)	(3) $Dec._{J2000}$ (° ' ")	(4) $S_{1.28\ GHz}$ (mJy)	(5) Resolved
J1131–1959b	11:31:55.60	−19:59:33.2	0.40 ± 0.17	Y
J1131–2008	11:31:55.72	−20:08:18.7	0.99 ± 0.09	Y
J1131–2014	11:31:55.76	−20:14:45.5	1.43 ± 0.09	Y
J1131–2002	11:31:57.47	−20:02:30.6	0.35 ± 0.15	Y
J1131–1946c	11:31:58.17	−19:46:56.5	0.29 ± 0.10	Y
J1131–2020	11:31:58.43	−20:20:41.1	0.30 ± 0.17	Y
J1131–2007b	11:31:58.69	−20:07:00.6	0.40 ± 0.14	Y
J1131–1943b	11:31:58.81	−19:43:53.0	1.53 ± 0.09	Y
J1132–1954	**11:32:02.77**	**−19:54:09.0**	**1.02 ± 0.10**	**Y (12)**
J1132–1941	11:32:03.39	−19:41:43.1	0.88 ± 0.09	Y
J1132–1952	**11:32:04.16**	**−19:52:11.1**	**0.25 ± 0.05**	**N**
J1132–1926	11:32:04.73	−19:26:17.5	1.09 ± 0.15	Y
J1132–2011	11:32:06.33	−20:11:25.9	1.49 ± 0.08	Y
J1132–2023	11:32:10.98	−20:23:23.2	0.88 ± 0.15	Y
J1132–1956	11:32:13.96	−19:56:09.3	0.69 ± 0.09	Y
J1132–2007	11:32:14.79	−20:07:38.9	0.50 ± 0.09	Y
J1132–2003a	11:32:21.68	−20:03:09.8	2.19 ± 0.08	Y
J1132–1951	11:32:21.71	−19:51:41.3	0.86 ± 0.10	Y
J1132–2022	11:32:22.73	−20:22:35.3	7.96 ± 0.21	Y
J1132–1949a	11:32:24.85	−19:49:01.1	0.50 ± 0.19	Y
J1132–1930	11:32:27.09	−19:30:35.7	20.2 ± 0.16	N
J1132–1948	11:32:30.09	−19:48:47.0	0.72 ± 0.08	N
J1132–1948b	11:32:31.26	−19:48:40.0	2.17 ± 0.22	Y
J1132–1952	11:32:34.77	−19:52:43.5	0.25 ± 0.11	Y
J1132–2022	11:32:28.57	−20:22:54.7	24.00 ± 0.0	Y
J1132–2003b	11:32:37.60	−20:03:57.8	1.50 ± 0.09	N
J1132–1949b	11:32:37.89	−19:49:08.7	6.19 ± 0.10	Y
J1132–1934	11:32:37.94	−19:34:47.5	1.81 ± 0.11	N
J1132–2019	11:32:39.35	−20:19:38.9	1.52 ± 0.11	N
J1132–2012	11:32:39.67	−20:12:05.9	1.16 ± 0.10	Y
J1132–2006	11:32:41.53	−20:06:54.1	9.10 ± 0.17	Y
J1132–2002	11:32:43.84	−20:02:53.7	4.08 ± 0.11	Y
J1132–2020	11:32:46.00	−20:20:57.7	1.11 ± 0.14	Y
J1132–1957	11:32:48.41	−19:57:55.5	0.60 ± 0.24	Y
J1132–2004	11:32:59.85	−20:04:02.7	7.47 ± 0.11	Y
J1133–2012	11:33:03.79	−20:12:09.7	6.70 ± 0.14	Y
J1133–2018	11:33:06.39	−20:18:55.7	1.98 ± 0.13	N
J1133–1952	11:33:07.67	−19:52:04.5	0.82 ± 0.12	Y
J1133–1951	11:33:08.33	−19:51:01.7	0.20 ± 0.09	Y
J1133–2011	11:33:09.56	−20:11:47.7	2.50 ± 0.14	N
J1133–2007	11:33:11.27	−20:07:14.4	1.05 ± 0.15	N
J1133–1945	11:33:13.05	−19:45:31.1	1.24 ± 0.11	Y
J1133–2004	11:33:18.09	−20:04:24.5	35.2 ± 0.36	Y
J1133–2016	11:33:20.76	−20:16:04.0	1.38 ± 0.19	Y
J1133–2002	11:33:26.29	−20:02:13.3	2.61 ± 0.26	Y
J1133–1940	11:33:32.94	−19:40:22.4	4.45 ± 0.15	Y
J1133–1959	11:33:33.89	−19:59:58.5	4.78 ± 0.29	Y
J1133–1954	11:33:36.91	−19:54:14.5	1299.1 ± 2.5	Y
J1133–1959	11:33:47.10	−19:59:05.2	0.29 ± 0.10	Y
J1133–1958	11:33:57.62	−19:58:00.0	0.20 ± 0.08	Y

Downloaded from https://academic.oup.com/mnras/article/504/2/2924/6219094 by CNR BOLOGNA AREA DELLA RICERCA user on 17 March 2022

Table A2. Same as Table A1, but for MACS J1931.8−2634 (cluster members in boldface).

(1) Name	(2) RA_{J2000} (hms)	(3) $Dec._{J2000}$ (° ' ")	(4) $S_{1.28\,GHz}$ (mJy)	(5) Resolved
J1929–2627	19:29:48.89	−26:27:32.3	0.56 ± 0.07	Y
J1929–2637	19:29:53.28	−26:37:44.7	2.00 ± 0.09	Y
J1930–2625a	19:30:00.09	−26:25:52.0	0.30 ± 0.04	Y
J1930–2631a	19:30:04.98	−26:31:46.0	0.35 ± 0.10	Y
J1930–2623a	19:30:05.88	−26:23:38.5	0.80 ± 0.08	Y
J1930–2616a	19:30:09.21	−26:16:24.2	0.54 ± 0.13	Y
J1930–2640	19:30:09.35	−26:40:42.9	0.78 ± 0.07	Y
J1930–2634	19:30:09.38	−26:34:28.8	0.45 ± 0.09	Y
J1930–2637	19:30:12.67	−26:37:25.7	0.26 ± 0.11	Y
J1930–2650	19:30:12.88	−26:50:49.0	1.71 ± 0.09	Y
J1930–2613	19:30:13.82	−26:13:35.5	0.97 ± 0.07	Y
J1930–2619	19:30:16.26	−26:19:26.9	0.80 ± 0.07	Y
J1930–2644a	19:30:16.75	−26:44:30.3	1.53 ± 0.08	Y
J1930–2621	19:30:16.92	−26:21:56.6	0.94 ± 0.07	Y
J1930–2631b	19:30:18.81	−26:31:12.3	8.29 ± 0.13	Y
J1930–2624a	19:30:19.86	−26:24:11.6	0.31 ± 0.08	Y
J1930–2630	19:30:21.29	−26:30:01.3	2.86 ± 0.11	Y
J1930–2628	19:30:22.94	−26:28:41.6	1.13 ± 0.07	Y
J1930–2643	19:30:25.36	−26:43:40.4	3.85 ± 0.08	Y
J1930–2626a	19:30:25.52	−26:26:28.7	2.65 ± 0.08	Y
J1930–2611	19:30:28.42	−26:11:29.5	0.25 ± 0.12	Y
J1930–2626b	19:30:30.88	−26:26:24.1	0.70 ± 0.09	Y
J1930–2623b	19:30:37.88	−26:23:27.0	0.27 ± 0.11	Y
J1930–2624b	19:30:37.95	−26:24:47.9	0.49 ± 0.09	Y
J1930–2643	19:30:38.23	−26:43:11.4	27.10 ± 0.30	Ext. FRII
J1930–2625b	19:30:38.38	−26:25:06.6	0.38 ± 0.11	Y
J1930–2647a	19:30:38.45	−26:47:16.1	2.13 ± 0.14	Y
J1930–2629	19:30:39.43	−26:29:13.6	0.75 ± 0.08	Y
J1930–2653	19:30:43.65	−26:53:45.9	0.84 ± 0.09	Y
J1930–2647b	19:30:44.07	−26:47:34.8	0.93 ± 0.09	Y
J1930–2628	19:30:45.91	−26:28:23.1	0.58 ± 0.10	Y
J1930–2644b	19:30:47.62	−26:44:15.3	54.80 ± 0.70	Y
J1930–2633	19:30:48.46	−26:33:39.8	0.69 ± 0.08	Y
J1930–2631c	19:30:50.58	−26:31:52.8	0.71 ± 0.10	Y
J1930–2658	19:30:53.09	−26:58:00.7	0.29 ± 0.04	Y
J1930–2610	19:30:53.48	−26:10:37.6	0.29 ± 0.12	Y
J1930–2650	19:30:54.68	−26:50:50.5	2.80 ± 0.08	Y
J1930–2655	19:30:55.04	−26:55:37.8	0.72 ± 0.08	Y
J1930–2620	19:30:55.36	−26:20:48.4	12.60 ± 0.20	Y
J1930–2616b	19:30:56.61	−26:16:56.6	2.00 ± 0.08	Y
J1930–2636	19:30:57.98	−26:36:14.6	1.70 ± 0.08	Y
J1930–2617	19:30:59.18	−26:17:33.9	0.47 ± 0.10	Y
J1930–2626c	19:30:59.84	−26:26:40.8	0.30 ± 0.08	Y
J1931–2616	19:31:00.24	−26:16:45.8	0.43 ± 0.10	Y
J1931–2607	19:31:00.29	−26:07:41.4	1.04 ± 0.07	Y
J1931–2629	19:31:03.06	−26:29:00.8	0.40 ± 0.08	Y
J1931–2620	19:31:03.58	−26:20:25.0	7.40 ± 0.10	Y
J1931–2656a	19:31:05.65	−26:56:40.6	0.51 ± 0.1	Y
J1931–2608a	19:31:06.99	−26:08:09.2	0.29 ± 0.12	Y
J1931–2640	19:31:07.24	−26:40:59.0	0.93 ± 0.08	Y
J1931–2613a	19:31:09.22	−26:13:04.0	0.30 ± 0.13	Y
J1931–2644	19:31:17.19	−26:44:48.9	28.40 ± 0.30	Y
J1931–2608b	19:31:17.54	−26:08:44.5	1.20 ± 0.07	Y
J1931–2630	19:31:18.34	−26:30:18.4	0.30 ± 0.05	N
J1931–2630a	19:31:19.36	−26:30:17.4	0.38 ± 0.11	Y
J1931–2656b	19:31:20.25	−26:56:29.7	0.67 ± 0.09	Y
J1931–2640	19:31:20.53	−26:40:46.9	0.59 ± 0.09	Y
J1931–2659	19:31:27.54	−26:59:30.7	1.47 ± 0.14	Y
J1931–2618	19:31:28.04	−26:18:46.2	1.10 ± 0.08	Y
J1931–2651	19:31:30.40	−26:51:23.5	0.41 ± 0.13	Y
J1931–2619	19:31:30.62	−26:19:58.6	11.1 ± 0.18	Y
J1931–2655	19:31:32.41	−26:55:45.3	3.71 ± 0.08	Y

Downloaded from https://academic.oup.com/mnras/article/504/2/2924/6219094 by CNR BOLOGNA AREA DELLA RICERCA user on 17 March 2022

Table A2 – *continued*

(1) Name	(2) RA_{J2000} (hms)	(3) $Dec._{J2000}$ (° ' ")	(4) $S_{1.28\ GHz}$ (mJy)	(5) Resolved
J1931–2654a	19:31:35.79	−26:54:52.3	0.39 ± 0.11	Y
J1931–2633	19:31:36.44	−26:33:09.6	14.5 ± 0.13	Y
J1931–2613b	19:31:38.92	−26:13:13.6	1.50 ± 0.08	Y
J1931–2617	19:31:43.67	−26:17:42.2	1.17 ± 0.07	Y
J1931–2654b	19:31:45.51	−26:54:24.2	0.23 ± 0.10	Y
J1931–2637	**19:31:46.60**	**−26:37:31.7**	**0.39 ± 0.04**	**N**
J1931–2634	**19:31:49.58**	**−26:34:32.7**	**45.40 ± 0.80**	**Ext. BCG**
J1931–2635	**19:31:50.02**	**−26:35:17.2**	**145.20 ± 0.70**	**Ext. NAT**
J1931–2656	19:31:50.81	−26:56:11.6	0.50 ± 0.14	Y
J1931–2624	19:31:51.96	−26:24:27.0	0.84 ± 0.09	Y
J1931–2630b	**19:31:54.86**	**−26:30:57.7**	**0.88 ± 0.10**	**N**
J1931–2622a	19:31:57.36	−26:22:09.6	0.79 ± 0.1	Y
J1931–2645a	19:31:57.54	−26:45:37.4	0.40 ± 0.05	N
J1931–2645	**19:31:58.33**	**−26:45:34.4**	**0.25 ± 0.05**	**N**
J1931–2622b	19:31:58.65	−26:22:27.5	0.49 ± 0.08	Y
J1931–2638	19:31:58.92	−26:38:15.7	3.40 ± 0.09	Y
J1932–2654a	19:32:00.42	−26:54:17.6	1.08 ± 0.09	Y
J1932–2620	19:32:03.09	−26:20:11.3	0.59 ± 0.16	Y
J1932–2632	19:32:05.17	−26:32:05.5	0.48 ± 0.11	Y
J1932–2627a	19:32:05.18	−26:27:00.2	2.29 ± 0.13	Y
J1932–2646	19:32:06.44	−26:46:31.2	0.48 ± 0.09	Y
J1932–2621a	19:32:07.11	−26:21:05.1	0.60 ± 0.09	Y
J1932–2625	**19:32:07.42**	**−26:25:16.3**	**0.25 ± 0.05**	**N**
J1932–2702	19:32:07.72	−27:02:28.1	0.33 ± 0.07	Y
J1932–2627b	19:32:08.17	−26:27:03.6	0.52 ± 0.10	Y
J1931–2625	19:32:09.72	−26:25:29.6	0.30 ± 0.05	N
J1932–2621b	19:32:10.80	−26:21:50.4	1.74 ± 0.12	Y
J1932–2634	19:32:11.31	−26:34:01.2	0.32 ± 0.09	Y
J1932–2657a	19:32:11.48	−26:57:08.6	1.16 ± 0.08	Y
J1932–2618a	19:32:11.85	−26:18:43.7	2.20 ± 0.13	Y
J1932–2637	19:32:12.16	−26:37:30.1	0.33 ± 0.07	Y
J1932–2648a	19:32:12.23	−26:48:18.1	0.69 ± 0.07	Y
J1932–2633a	19:32:12.53	−26:33:14.4	0.90 ± 0.09	Y
J1932–2628a	19:32:12.95	−26:28:07.8	0.32 ± 0.08	Y
J1932–2654b	19:32:14.00	−26:54:24.0	0.47 ± 0.12	Y
J1932–2651	19:32:14.41	−26:51:39.6	0.47 ± 0.13	Y
J1932–2648b	19:32:16.55	−26:48:44.9	0.40 ± 0.10	Y
J1932–2608	19:32:16.77	−26:08:22.2	4.30 ± 0.07	Y
J1932–2629	19:32:17.70	−26:29:32.1	1.50 ± 0.09	Y
J1932–2621c	19:32:18.84	−26:21:26.1	0.30 ± 0.09	Y
J1932–2618b	19:32:19.56	−26:18:15.1	0.44 ± 0.09	Y
J1932–2631	19:32:20.07	−26:31:35.2	0.50 ± 0.06	N
J1932–2659	19:32:21.12	−26:59:02.7	0.39 ± 0.13	Y
J1932–2644	19:32:21.41	−26:44:20.6	0.74 ± 0.14	Y
J1932–2654c	19:32:25.41	−26:54:26.0	2.10 ± 0.09	Y
J1932–2648c	19:32:25.80	−26:48:16.4	0.79 ± 0.09	Y
J1932–2632	19:32:26.13	−26:32:48.8	0.50 ± 0.07	N
J1932–2633b	19:32:27.31	−26:33:10.4	17.40 ± 0.20	Y
J1932–2613	19:32:29.01	−26:13:24.3	0.44 ± 0.09	Y
J1932–2628b	19:32:30.33	−26:28:10.2	0.43 ± 0.10	Y
J1932–2628c	19:32:30.69	−26:28:50.9	0.60 ± 0.11	Y
J1932–2624	19:32:30.76	−26:24:35.8	0.42 ± 0.10	Y
J1932–2628d	19:32:30.92	−26:28:03.3	0.85 ± 0.11	Y
J1932–2641	19:32:31.01	−26:41:51.4	0.56 ± 0.08	Y
J1932–2631a	19:32:31.57	−26:31:20.8	0.50 ± 0.06	N
J1932–2627c	19:32:31.76	−26:27:58.9	1.10 ± 0.18	Y
J1932–2654d	19:32:31.78	−26:54:36.2	0.65 ± 0.09	Y
J1932–2639a	19:32:33.34	−26:39:08.1	0.60 ± 0.10	Y
J1932–2617	19:32:36.58	−26:17:11.1	0.29 ± 0.18	Y
J1932–2618c	19:32:40.26	−26:18:54.8	6.40 ± 0.09	Y
J1932–2645	19:32:40.28	−26:45:47.1	0.47 ± 0.07	Y
J1932–2658	19:32:41.09	−26:58:37.8	3.50 ± 0.10	Y
J1932–2635	19:32:41.52	−26:35:58.4	1.23 ± 0.11	Y

Downloaded from https://academic.oup.com/mnras/article/504/2/2924/6219094 by CNR BOLOGNA AREA DELLA RICERCA user on 17 March 2022

Table A2 *– continued*

(1) Name	(2) RA_{J2000} (hms)	(3) $Dec._{J2000}$ (° ' ")	(4) $S_{1.28\,GHz}$ (mJy)	(5) Resolved
J1932–2657b	19:32:43.01	−26:57:54.5	0.85 ± 0.08	Y
J1932–2630	19:32:44.91	−26:30:13.3	57.80 ± 0.30	Y
J1932–2639b	19:32:44.93	−26:39:32.5	0.43 ± 0.11	Y
J1932–2638a	19:32:46.69	−26:38:52.2	0.42 ± 0.11	Y
J1932–2638b	19:32:47.75	−26:38:47.3	0.83 ± 0.08	N
J1932–2656	19:32:49.35	−26:56:06.7	0.49 ± 0.22	Y
J1932–2642	19:32:51.32	−26:42:51.1	6.10 ± 0.09	Y
J1932–2616	19:32:57.12	−26:16:41.9	0.60 ± 0.08	Y
J1932–2636	19:32:58.43	−26:36:50.5	1.60 ± 0.09	Y
J1932–2643	19:32:58.68	−26:43:29.7	5.30 ± 0.09	Y
J1933–2618	19:33:04.09	−26:18:01.8	0.71 ± 0.15	Y
J1933–2617	19:33:04.44	−26:17:05.4	0.45 ± 0.10	Y
J1933–2630	19:33:05.31	−26:30:04.7	1.47 ± 0.09	Y
J1933–2658	19:33:05.51	−26:58:20.8	5.30 ± 0.20	Y
J1933–2622	19:33:06.31	−26:22:22.9	12.3 ± 0.1	Y
J1933–2652	19:33:06.37	−26:52:35.7	0.80 ± 0.11	Y
J1933–2656	19:33:10.77	−26:56:26.2	0.93 ± 0.10	Y
J1933–2649	19:33:12.35	−26:49:15.0	0.31 ± 0.08	Y
J1933–2613	19:33:14.23	−26:13:22.9	27.60 ± 0.20	Y
J1933–2624a	19:33:17.35	−26:24:15.5	0.50 ± 0.05	Y
J1933–2631	19:33:19.13	−26:31:30.7	1.24 ± 0.11	Y
J1933–2640	19:33:19.22	−26:40:31.4	6.00 ± 0.11	Y
J1933–2624b	19:33:23.12	−26:24:02.8	0.81 ± 0.11	Y
J1933–2614	19:33:27.28	−26:14:53.9	1.30 ± 0.09	Y
J1933–2634	19:33:27.33	−26:34:04.0	1.40 ± 0.14	Y
J1933–2626	19:33:28.07	−26:26:00.8	1.64 ± 0.09	Y
J1933–2650	19:33:28.26	−26:50:03.9	0.37 ± 0.11	Y
J1933–2618	19:33:28.99	−26:18:34.3	1.13 ± 0.09	Y
J1933–2629	19:33:30.66	−26:29:14.8	6.02 ± 0.18	Y
J1933–2652	19:33:31.35	−26:52:16.8	0.69 ± 0.14	Y
J1933–2642	19:33:35.87	−26:42:44.8	1.12 ± 0.10	Y
J1933–2643	19:33:38.55	−26:43:13.9	0.55 ± 0.08	Y
J1933–2646	19:33:39.12	−26:46:23.9	0.77 ± 0.09	Y
J1933–2623	19:33:45.81	−26:23:41.1	0.83 ± 0.13	Y
J1933–2633	19:33:48.45	−26:33:16.4	748.4 ± 6.1	Ext. FRII
J1933–2645a	19:33:52.33	−26:45:33.1	4.50 ± 0.12	Y
J1933–2645b	19:33:52.53	−26:45:00.2	29.30 ± 0.20	Y

APPENDIX B: RADIO–OPTICAL CROSS ID

The radio optical cross-matches for MACS J1931.8−2634 and A 1300 are given in Tables B1 and B2, respectively.

Downloaded from https://academic.oup.com/mnras/article/504/2/2924/6219094 by CNR BOLOGNA AREA DELLA RICERCA user on 17 March 2022

Table B1. MACSJ1931.8−2634 radio–optical identifications (cluster members are in boldface). Left to right: radio source name; J2000 right ascension and declination from the radio image; J2000 right ascension and declination of the optical counterpart; B and Rc magnitudes; colour index, spectroscopic redshift, and MeerKAT flux density.

(1) Name	(2) RA_{J2000} (hms)	(3) $Dec._{J2000}$ (° ' ")	(4) RA_{opt} (hms)	(5) $Dec._{opt}$ (° ' ")	(6) B	(7) Rc	(8) $B-Rc$	(9) z_{spec}	(10) S_M (mJy)
J1930–2636	19:30:57.98	−26:36:14.6	19:30:57.97	−26:36:14.4	25.6	23.86	1.74	–	1.70 ± 0.08
J1931–2629	19:31:03.06	−26:29:00.8	19:31:03.04	−26:28:59.8	25.45	23.58	1.87	–	0.40 ± 0.08
J1931–2640	19:31:07.24	−26:40:59.0	19:31:07.24	−26:40:58.5	25.6	23.95	1.65	–	0.93 ± 0.08
J1931–2630	19:31:18.34	−26:30:18.4	19:31:18.30	−26:30:17.6	22.36	22.18	0.18	–	0.30 ± 0.05
J1931–2630	19:31:19.36	−26:30:17.4	19:31:19.33	−26:30:16.9	24.65	22.94	1.71	–	0.38 ± 0.11
J1931–2640	19:31:20.53	−26:40:46.9	19:31:20.51	−26:40:46.1	18.84	18.78	0.06	–	0.59 ± 0.09
J1931–2633	19:31:36.44	−26:33:09.6	19:31:36.43	−26:33:09.1	24.21	21.90	2.31	–	14.50 ± 0.13
J1931–2637	**19:31:46.60**	**−26:37:31.7**	**19:31:46.53**	**−26:37:31.0**	**21.95**	**19.67**	**2.28**	**0.342**	0.39 ± 0.04
J1931–2634	**19:31:49.58**	**−26:34:32.7**	**19:31:49.63**	**−26:34:32.6**	**18.84**	**18.14**	**0.70**	**0.352**	45.40 ± 0.80
J1931–2635	**19:31:50.02**	**−26:35:17.2**	**19:31:50.00**	**−26:35:17.1**	**21.50**	**19.20**	**2.27**	**0.351**	145.2 ± 0.7
J1931–2630b	**19:31:54.86**	**−26:30:57.7**	**19:31:54.86**	**−26:30:57.0**	**21.66**	**19.46**	**2.20**	**0.351**	0.88 ± 0.10
J1931–2645	19:31:57.54	−26:45:37.4	19:31:57.55	−26:45:37.4	24.37	22.92	1.45	–	0.40 ± 0.05
J1931–2645	**19:31:58.33**	**−26:45:34.4**	**19:31:58.32**	**−26:45:34.4**	**20.85**	**19.33**	**1.52**	**0.359**	0.25 ± 0.05
J1931–2638	19:31:58.92	−26:38:15.7	19:31:58.93	−26:38:15.2	23.50	22.08	1.42	–	3.40 ± 0.09
J1932–2632	19:32:05.17	−26:32:05.5	19:32:05.24	−26:32:05.8	24.49	24.41	0.08	–	0.48 ± 0.11
J1932–2625	**19:32:07.42**	**−26:25:16.4**	**19:32:07.45**	**−26:25:16.3**	**20.52**	**19.22**	**1.30**	**0.349**	0.25 ± 0.05
J1932–2625	19:32:09.72	−26:25:29.6	19:32:09.74	−26:25:28.8	22.61	21.47	1.14	–	0.30 ± 0.05
J1932–2637	19:32:12.16	−26:37:30.1	19:32:12.11	−26:37:29.5	20.07	18.81	1.26	0.207	0.33 ± 0.07
J1932–2629	19:32:17.70	−26:29:32.1	19:32:17.70	−26:29:31.6	22.33	20.31	2.02	–	1.50 ± 0.09
J1932–2631	19:32:20.07	−26:31:35.2	19:32:20.04	−26:31:34.4	19.90	18.86	1.04	0.145	0.50 ± 0.07
J1932–2632	19:32:26.13	−26:32:48.8	19:32:26.13	−26:32:48.4	21.80	20.22	1.58	–	0.50 ± 0.07
J1932–2633	19:32:27.71	−26:33:56.4	19:32:27.77	−26:33:55.6	25.6	24.16	1.44	–	17.40 ± 0.20
J1932–2628	19:32:30.92	−26:28:03.3	19:32:30.91	−26:28:02.8	25.98	22.33	3.65	–	0.85 ± 0.11
J1932–2641	19:32:31.01	−26:41:51.4	19:32:31.04	−26:41:51.1	25.6	24.20	1.4	–	0.56 ± 0.08
J1932–2631	19:32:31.57	−26:31:20.8	19:32:31.61	−26:31:20.4	24.24	23.49	0.75	–	0.50 ± 0.06

Table B2. A1300 radio–optical identifications (cluster members in boldface). Left to right: radio source name; J2000 right ascension and declination from the radio image; J2000 right ascension and declination of the optical counterpart; *g'* and *r'* magnitudes; colour index; spectroscopic redshift and MeerKAT flux density).

(1) Name	(2) RA_{J2000} (hms)	(3) $Dec._{J2000}$ (° ' ")	(4) RA_{opt} (hms)	(5) $Dec._{opt}$ (° ' ")	(6) g'	(7) r'	(8) $g'-r'$	(9) z_{spec}	(10) S_M (mJy)
J1131–1959	11:31:09.25	−19:59:19.0	11:31:09.25	−19:59:19.9	23.34	22.26	1.07	–	4.20 ± 0.08
J1131–2000	**11:31:13.74**	**−20:00:20.5**	**11:31:13.73**	**−20:00:21.5**	**21.35**	**19.95**	**1.40**	**0.303**	1.95 ± 0.11
J1131–1947	11:31:22.48	−19:47:31.2	11:31:22.47	−19:47:32.8	25.55	23.21	2.33	–	0.47 ± 0.09
J1131–2001	11:31:24.77	−20:01:09.5	11:31:24.75	−20:01:10.6	25.55	24.15	1.39	–	10.30 ± 0.10
J1131–1953	11:31:26.89	−19:53:26.1	11:31:26.90	−19:53:27.3	21.98	21.95	0.02	3.020	3.91 ± 0.08
J1131–1951	11:31:27.51	−19:51:46.1	11:31:27.52	−19:51:47.8	25.55	23.79	1.75	–	1.36 ± 0.09
J1131–1946	11:31:32.53	−19:46:59.4	11:31:32.52	−19:47:00.0	22.01	20.78	1.22	–	0.63 ± 0.07
J1131–1952	11:31:43.92	−19:52:54.3	11:31:43.84	−19:52:45.8	20.24	18.89	1.34	0.257	16.20 ± 0.10
J1131–1954	**11:31:46.79**	**−19:54:52.5**	**11:31:47.13**	**−19:54:52.7**	**21.05**	**19.63**	**1.41**	**0.302**	0.25 ± 0.05
J1131–1950	11:31:48.42	−19:50:43.8	11:31:48.41	−19:50:45.2	23.33	22.64	0.69	–	0.70 ± 0.08
J1131–1949	**11:31:48.62**	**−19:49:01.7**	**11:31:48.56**	**−19:49:02.2**	**21.23**	**20.21**	**1.02**	**0.302**	0.25 ± 0.05
J1131–1958	**11:31:49.50**	**−19:58:07.9**	**11:31:49.53**	**−19:58:07.6**	**20.87**	**19.74**	**1.13**	**0.295**	0.39 ± 0.05
J1131–1953b	**11:31:54.30**	**−19:53:53.5**	**11:31:54.27**	**−19:53:50.8**	**20.86**	**19.41**	**1.45**	**0.305**	37.80 ± 0.40
J1131–1955	**11:31:54.34**	**−19:55:39.0**	**11:31:54.18**	**−19:55:39.8**	**20.09**	**18.62**	**1.46**	**0.307**	12.10 ± 0.16
J1131–1952b	**11:31:54.85**	**−19:52:07.7**	**11:31:54.95**	**−19:52:10.2**	**20.70**	**19.24**	**1.45**	**0.303**	2.30 ± 0.13
J1131–1959	11:31:55.60	−19:59:33.2	11:31:55.46	−19:59:34.2	25.53	23.12	2.43	0.740	0.40 ± 0.17
J1131–2002	11:31:57.47	−20:02:30.5	11:31:57.40	−20:02:32.1	21.93	20.78	1.14	–	0.35 ± 0.15
J1131–1946	11:31:58.17	−19:46:56.5	11:31:58.19	−19:46:58.2	22.09	20.42	1.66	0.227	0.29 ± 0.10
J1132–1954	**11:32:02.77**	**−19:54:09.0**	**11:32:02.70**	**−19:54:13.5**	**21.23**	**19.78**	**1.44**	**0.306**	1.02 ± 0.10
J1132–1952	**11:32:04.16**	**−19:52:11.1**	**11:32:04.41**	**−19:52:11.1**	**21.14**	**20.39**	**0.74**	**0.302**	0.25 ± 0.05
J1132–1956	11:32:13.96	−19:56:09.2	11:32:14.02	−19:56:10.9	25.55	23.26	2.29	–	0.69 ± 0.09
J1132–1951	11:32:21.71	−19:51:41.3	11:32:21.71	−19:51:42.9	25.55	23.56	1.98	–	0.86 ± 0.10
J1132–1949	11:32:24.85	−19:49:01.1	11:32:24.84	−19:49:02.3	24.04	22.19	1.84	–	0.50 ± 0.19
J1132–1948	11:32:30.09	−19:48:47.0	11:32:30.08	−19:48:48.4	23.68	21.96	1.72	–	0.72 ± 0.08
J1132–1948	11:32:31.26	−19:48:40.0	11:32:31.30	−19:48:41.8	23.62	21.87	1.74	–	2.17 ± 0.22
J1132–1952	11:32:34.77	−19:52:43.5	11:32:34.73	−19:52:45.0	18.27	18.24	0.03	0.389	0.25 ± 0.11

This paper has been typeset from a TEX/LATEX file prepared by the author.

Downloaded from https://academic.oup.com/mnras/article/504/2/2924/6219094 by CNR BOLOGNA AREA DELLA RICERCA user on 17 March 2022